



ADVANCED REMOTE SENSING JOURNAL

Volume 1 Issue 1 DECEMBER 2021



ADVANCED REMOTE SENSING

(VOLUME: 1, ISSUE: 1)

DECEMBER, 2021

Aim

[Advanced Remote Sensing Journal \(ARSEJ\)](#) publishes regular research papers, reviews, letters, and communications covering all aspects of remote sensing science, from sensor design, validation/calibration, to its application in geosciences, environmental sciences, ecology, and civil engineering. Our aim is to publish novel / improved methods/approaches and/or algorithms of remote sensing to benefit the community, open to everyone in need of them. There is no restriction on the length of the papers or colors used. The method/approach must be presented in detail so that the results can be reproduced. There are, in addition, three unique features of this Journal:

- Manuscripts regarding research proposals and research ideas are welcome
- Electronic files and software regarding the full details of the calculation and experimental procedure, if unable to be published in a normal way, can be deposited as supplementary material
- We also accept manuscripts communicating to a broader audience with regard to research projects financed with public funds

[\(ARSEJ\)](#) is a **Blind Review** and a **free journal**. All of the responsibilities belong to authors.

Scope

Basic remote sensing applications

Multi-spectral and Hyperspectral remote sensing

Active and passive microwave remote sensing (RADAR/SAR)

Lidar and laser scanning

Geometric reconstruction

Image classification and analysis methods

Image processing and pattern recognition

Data fusion and data assimilation

Improvement of atmospheric modelling for radiometric correction

Modelling of parameters obtained from satellite data

Global modelling, monitoring and global database for sustainable development

Checking validity of data by using laboratory and in-situ test methods

Integration of remote sensing and GIS methods

Information utility for reducing disaster and risk effects: Early warning system, Impact assessment, monitoring, flexibility and risk reduction studies

Environmental pollution: Assessment and impact studies

Integration of remote sensing inputs and Earth surface applications

Monitoring growth of agricultural products for sustainable agriculture

Physical modeling and signatures

Change detection

Climate change studies

Global and regional dynamic of land use/biodiversity

Desertification and aridity studies

Soil, vegetation and carbon arc in shore and ocean water

Water quality studies

Dedicated satellite missions

Operational processing facilities

Spaceborne, airborne, unmanned aerial vehicle (UAV) and terrestrial platforms

EDITORIAL BOARD

Editor

Prof. Dr. Murat Yakar, Mersin University, Department of Geomatics Engineering (myakar@mersin.edu.tr)

Co-Editor

Prof. Lachezar Hristov Filchev, Bulgarian Academy of Sciences, Bulgaria (lachezarhf@gmail.com)

Editorial Board

Prof. Mohamed Fouad Abdel Aziz Soliman, Arish University, Faculty of Arts, Egypt (mi_me46@yahoo.com)
(mohamed.fouad2005@yahoo.com)

Dr. Mohamed Atallah (atallahm763@gmail.com)

Prof. *Muhammed Bilal*, School of Marine Sciences, Nanjing University of Information Science & Technology, China (muhammad.bilal@connect.polyu.hk)

Assoc. Prof. Dr. Abel Ramoelo, University of Pretoria, South Africa (abel.ramoelo@gmail.com)

Prof. Dr. Khalil VALIZADEH KAMRAN, University of Tabriz, Faculty of Planning and Environmental Sciences, Iran (valizadeh@tabrizu.ac.ir)

Assoc. Prof. Dr. Eng. Ahmed Serwa, Mataria Helwan University, ahmed_serwa@yahoo.com

Asst. Prof. Atta-ur-Rahman, University of Peshawar, Pakistan (atta-ur-rehman@uop.edu.pk)

Asst. Prof. Ghani Rahman, University of Gujrat, Pakistan (ghanigeo@gmail.com)

Abdell Aziiz Fatthii Abdell Aziiz Ellfadally, Basilicata University / Italian National Research Councils/ National Authority for Remote Sensing and Space Sciences, Italy (abdelaziz.elfadaly@narss.sci.eg) / (abdelaziz.elfadaly@imaa.cnr.it)

Asst. Prof. Dr. KAMAL SROGY DARWISH, Minia University, Egypt (kamal.srogy@mu.edu.eg / kamalelsrogy@gmail.com)

Dr. Milad Janalipour Toosi University of Tech., Tehran – Iran (milad_janalipour@ari.ac.ir)

Asst. Prof. Dr. Mustafa ÜSTÜNER (Artvin Çoruh University) mustuner@artvin.edu.tr

Mohamed Ahmed Badawi Attallah (atallahm763@gmail.com) (atallahm763@gmail.com)

Bello Abubakar Abubakar, Geography Teacher, Islamic Learning Centre (abubakarbello1064@gmail.com)

Dr. Mamadou TRAORE, Central African Republic (matraba77@gmail.com)

Dr. Hashir Tanveer, University of Alabama (hashirrana3@gmail.com)

Dr. AQIL TARIQ (Wuhan University, Wuhan 430079, China) State Key Laboratory of Information Engineering in Surveying Mapping and Remote Sensing (LIESMARS) (aqiltariq@whu.edu.cn /aqiltariq85@gmail.com)

Dr. Sawaid ABBAS (The Hong Kong Polytechnic University, Hong Kong) (sawaid.abbas@gmail.com; sawaid.abbas@connect.polyu.hk)

Dr. Thapa Pawan (Kathmandu University, Dhulikhel, Nepal) pawan.thapa@ku.edu.np

Contents

Dramatically increase of built-up area in Iraq during the last four decades	1-9
<i>Azad Othman Rasul, Hasan Mohammed Hameed, Gaylan Rasul Faqe Ibrahim</i>	
Crop classification from multi-temporal PolSAR data with regularized greedy forest	10-15
<i>Mustafa Ustuner, Fusun Balik Sanli</i>	
Performance analysis of YOLO versions for automatic vehicle detection from UAV images	16-30
<i>Melis Uzar, Şennur Öztürk, Onur Can Bayrak, Tümay Arda, Nursu Tunalioglu Öcalan</i>	
Evaluation of the relationship between urban area and land surface temperature determined from optical satellite data: A case of Istanbul	31-37
<i>Gülcan Sarp, Emre Baydoğan, Firdevs Güzel, Tuğba Otlukaya</i>	
LST change for 16-year period for different land use classes	38-45
<i>Burak Kotan, Abdullah Tatmaz, Suat Kılıç, Arzu Erener</i>	



Dramatically increase of built-up area in Iraq during the last four decades

Azad Othman Rasul¹, Hasan Mohammed Hameed², Gaylan Rasul Faqe Ibrahim^{1,3}

¹Soran University, Department of Geography, Iraq, azad.rasul@soran.edu.iq

²Soran University, Department of Civil Engineering, Iraq, hasan.hamid@soran.edu.iq

³University of Halabja, Department of Geography, Iraq, gailan.faqe@soran.edu.iq

Cite this study: Rasul, A. O., Hameed, H. M., & Ibrahim, G. R. F. (2021). Dramatically increase of built-up area in Iraq during the last four decades. *Advanced Remote Sensing*, 1(1), 1-9

Keywords

Land Use Land Cover (LULC)
Landsat
Google Earth Engine (GEE)
Iraq
Change detection
Random Forest

Research Article

Received: 11.11.2021
Revised: 04.12.2021
Accepted: 16.12.2021
Published: 30.12.2021

Abstract

Land Use Land Cover (LULC) detection is a crucial indicator of environmental change since it is associated with the climate, ecosystem procedures, land degradation, biodiversity and increased human actions. The objective of current study is to observe how main LULC class changed in Iraq from 1982 to 2019. Overall, 5259 Landsat 4, 5 and 8 images were utilized for land classification. In the study, Random Forest classification method was performed in Google Earth Engine (GEE) platform. The research has established the accuracy assessment of overall accuracy and kappa coefficient of four periods are 95% or higher. The trend of classes demonstrated that built up class increased dramatically by 248.6%. In contrast, bare soil, which covers most territories of Iraq decreased by 8.4% (30,212 km²) from Period 1(1982-1989) to Period 4 (2010-2019). Likewise, vegetation class decreased by 20.2% (8,151 km²) during the same period.

1. Introduction

Land is a significant natural resource, which covers the solid feature of the surface. Due to economic growth, land resources are now widely exploited in terms of industrial development, urban growth, and the conversion of forests to agricultural lands [1]. In recent decades, the subject of land use/land cover (LULC) has been a significant aspect of environmental change and climate change studies. LULC has a major impact on global modification due to its associations with the climate, ecosystem procedures, land degradation, biodiversity and increased human action [2]. The physical condition and biotic constituent of the earth surface are called land cover [3]. While alterations of land cover by man are called land use [4]. Determination of changes in physical land cover over a series of time is called change detection, which is the most significant aspect of environment alteration [5]. Furthermore, rapid modifications in LULC have caused a drastic drop in green area [6].

LULC is growing and changing rapidly around the world and this poses a very high risk to parts of the ecosystem such as water bodies, soil, and temperature, especially in urban centers [4]. Human actions have principally reflected the land cover change dynamics [7-8]. Atmospheric rotation, vegetation protection, biogeochemical and energy cycle are multiple processes of the earth that have an impact on the land cover changes [9]. Evaluation of LULC is a significant criterion for effectively planning land reserve management. It is a key component for up-to-date plans in protecting natural resources and observed changes in the environment which is assets to develop balance conservation strategies and enlargement pressure [10].

Urbanization plays an important role in LULC transition through the substitution of natural land cover for habituated area and vegetation for economic reasons and facilities. Urbanization involves changes in land cover by structural engineering constraints such as highways, houses [4]. Urban populations are expanded faster than rural places, with high migration levels in metropolitan sites. Urban dwellers were projected to be approximately (3) billion people, and it is predicted to rise to 60% by 2030.

The major driving forces for land use alteration are industrial development, urbanization, population growth and economic reforms [11]. LULC changes such as the abandonment of agricultural land are capable of being caused by an accelerated socio-economic alteration [12]. The researchers [13-14] demonstrate that political and socio-economic improvements influence urbanization. Their findings suggest that, in their case study, urban sites were key economic advancements. Political conflicts could have socio-economic, permanent or irrecoverable damage on cultivation. Thus, during the Iraq-Iran war of 1980-1988, the systematic desiccation of grassland led to devastating LCLU changes, biodiversity and human-induced operations. Not to mention that, in the period of 2003-2015, urbanization processes remarkably increased due to the socio-economic and political factors.

Currently, Google Earth Engine (GEE) is available as a powerful cloud computing platform that manages enormous volume of remote sensing data. It hosts a massive pool of remote sensing and geospatial datasets. In addition, a number of famous machine learning algorithms have been applied. Supervised classification is one of this filed. For instance, Decision Tree (DT), Support Vector Machine (SVM), and Random Forest (RF) classifier are available in the platform. Previous classification studies have demonstrated that RF outperformed and is easier than other classifiers such as DT. In addition, RF is overtraining and has presented high accuracies in several studies [15-19].

Satellite images were widely utilized to study temporary LULC shifts. The application of remote sensing data has been implemented and accepted as an effective detection method for identifying LULC change [20]. Image satellites are capable of providing reliable and relevant data for decision-makers in different fields concerning vegetation and crop production [21]. Researchers [22-25] utilized satellite images to analysis, monitor and measure the patterns of LULC changes, principally in large areas that experience rapid alterations in land use. Remote sensing data is a potentially powerful tool for detecting changes in LULC at higher temporal resolutions, reduced coasts, synoptic views, repetitive coverage and gaining real-time and conventional methods [26]. Numerous studies have validated the successive application of several satellites such as MODIS, Aster, Landsat [27-33]. The Landsat TM/ETM/OLI data have been broadly utilized for many research as an accessible remotely sensed data [34-40]. Despite the significant conversion of LULC classes in Iraq during last four decades, not sufficient study was conducted in this field at the country scale. Mostly, LULC study in Iraq focused on specific cities and they relied on a short period of satellite data. Therefore, the objective of current research is to observe how main LULC class changed in Iraq from 1982 to 2019.

2. Material and Method

2.1. Study area

Iraq is one of the Middle-Eastern countries located in southwestern Asia. It shares a boundary with Turkey from the north, Iran from the east, Syria and Jordan from the west, Saudi Arabia and Kuwait from the South (Figure 1). The total area of Iraq is 438,320 km² and the northern part of the study area are mountainous regions, which are about 3,550 m above the sea level. Whereas, the south part of the study area includes the desert area which covers around 40% of the total land of Iraq [41]. LULC is growing and changing rapidly around the world and this poses a very high risk to parts of the ecosystem such as water body, soil, and temperature, especially in urban centers [4].

Iraq has a unique climate; a Mediterranean climate combined with a subtropical semi-arid climate, especially in the north and northeastern parts. These areas are the first to experience precipitation in the November to April. However, December to February is precipitation season in the middle and south of the country. Mean annual precipitation is 216. The most rain is fall in the northeastern parts, which is around 1200 mm on average. Contrastingly, the southern parts receive 100 mm. July and August are the hottest months of summer, with temperatures reaching 43 °C in the shade. The temperature in winter days is 16 °C on average, dropping to around 2°C during nighttime [42].

Iraq includes nineteen governorates. Farmland makes up around 26% of the total area of the country while the remaining areas are unused. Agricultural and other areas that are sited on the extreme northern border with Turkey and Iraq is covered by forests and woodlands [43].

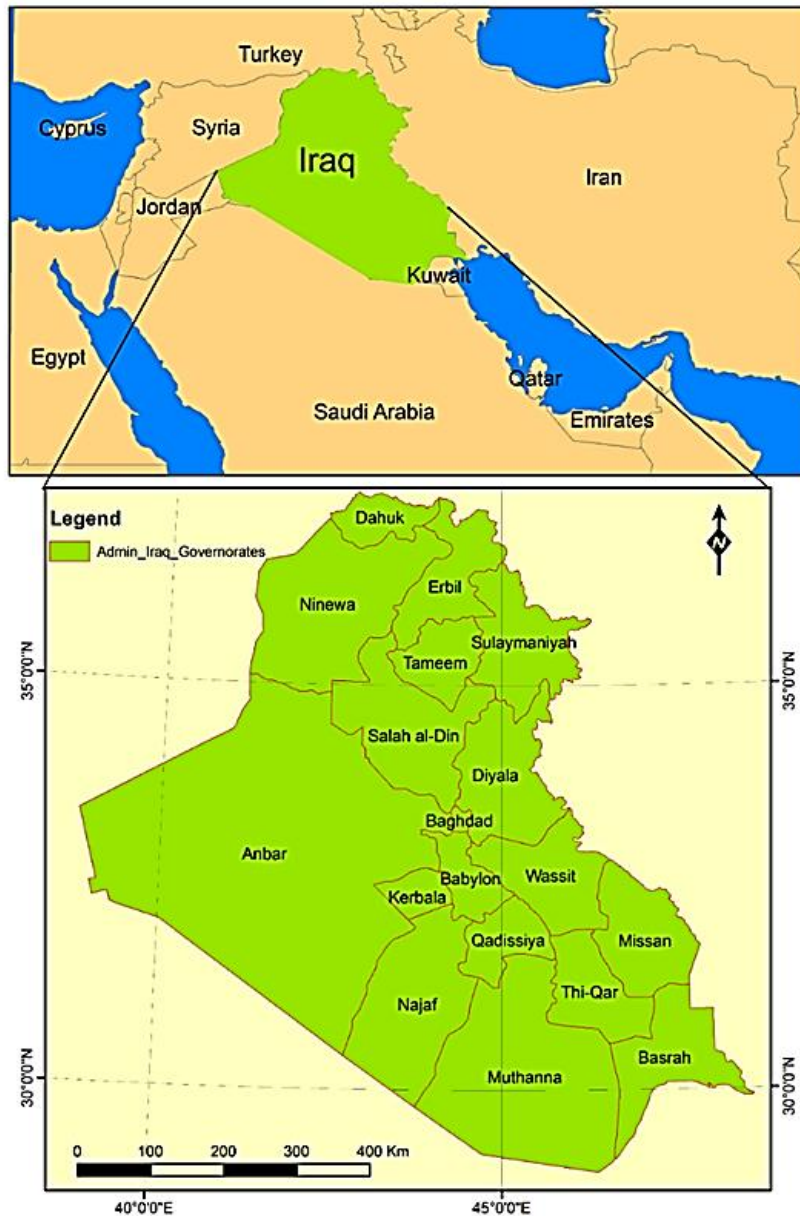


Figure 1. Location of the study area

2.2. Data

For the first period from 1982 to 1989, the study utilized 150 images of Landsat 4 (TM calibrated top-of-atmosphere reflectance, orthorectified scenes only.) less than 25% of cloud covers. For second period 1990 to 1999, we utilized 810 Landsat 5 (Landsat 5 TM calibrated top-of-atmosphere reflectance, orthorectified scenes only.) with less than 10% cloudy images. For third period from 2000 to 2009, 626 Landsat 5 images (less than 10% cloudy) were utilized. For the last period from 2010 to 2019, we utilized 3669 Landsat 8 images (Landsat 8 Collection 1 Tier 1 calibrated top-of-atmosphere (TOA) reflectance) less than 10% cloudy. Overall, 5259 Landsat images were utilized for classification in this study. With Landsat 4 and 5, bands 1 to 7 were selected and for Landsat 8, bands 2–7 and 10–11 were utilized in the study. For each period, the mean value between selected images was calculated. Then, mean images of all periods clipped to shapefile of Iraq.

2.3. LULC classes

In the current study, we were attended to exemplify the fundamental LULC classes of a landscape conversion in Iraq. We recognized four main LULC classes of interest: Bare soil, Built-up, waterbody (e.g., rivers, lake, dam) and vegetation (e.g., grass, trees, cropland, agriculture and pasture). For LULC conversion that is associated with urban growth, conversion of vegetation and bare soil to build up is important. Furthermore, these classes are

possible to identify in scale of Landsat images. The study period was divided into four periods; P1 from 1982 to 1989, P2 from 1990 to 1999, P3 from 2000 to 2009 and P4 from 2010 to 2019.

2.4. Methodology

GEE is utilized in this study for the images processing and performance of classification. The main steps are selecting images of Landsat within four periods; generating pixel-based mean value of each period, selecting samples of testing and validation points, producing classified maps, and post-classification to assess accuracy of classified maps.

2.4.1. Random forest classification.

In this research, the RF procedure was utilized for pixel-based LULC classifications because previous studies confirmed that the performance of RF is higher than other classifiers [44]. An RF is fundamentally an aggregate method that creates a multitude of decision trees and produces the mean prediction of the individual trees [45]. In our classification, 600 samples were selected for each period; 150 samples of each class. Samples are divided into two categories; 70% of samples utilized as training points and 30% of samples utilized as testing points for validation. In each period, we utilized an RF classifier with 10 decision trees. Classified images exported from GEE to Google Drive then downloaded.

2.4.2. Accuracy assessment

The accuracy of a classifier is the ability of method to properly classify a collection of samples. The data that utilized to experiment with the performance of the method should be different than the data utilized to train the classifier [46]. In case of inability of ground truth samples, for instance, samples of the land cover of previous decades, reference data is usually separated to training and experiment sets. Four evaluation classifier, overall accuracy (OA), Kappa coefficient, producer accuracy, and user accuracy were measured. Overall accuracy verifies the overall efficiency of the method that is calculated by dividing the total number of correctly considered samples by the total number of the testing samples. While, the Kappa coefficient demonstrates the degree of agreement between the validation data and the predicted values [47]. In this study, we utilized 30% of samples from 600 samples as testing points for validation. For accuracy assessment, Kappa and overall accuracy were derived by using error Matrix of classified image of each period. Then classified images were utilized in GIS tools to create a comparative figure of LULC classes during the different periods in the country.

3. Results and discussion

3.1. Accuracy assessment

Post classification comparison is utilized to demonstrate LULC changes between 5259 Landsat satellite images for different periods. LULC changes were extracted from Landsat images satellite for different periods. The accuracy assessment of overall accuracy and kappa coefficient are 98% and 97%, 96% and 95%, 98% and 97%, 99% and 99% in the first, second, third and fourth period, respectively, as demonstrated in [Table 1](#). The highest overall accuracy achieved was in 2010-2019 around 99%; moreover, the kappa coefficient for the same period was 99%. When kappa coefficient values are greater than 80% it represents strong agreement with the ground truth and this range is widely utilized as a minimum level of acceptable accuracy for LULC change classification [48].

Table 1. Accuracy assessment

Period	Overall accuracy	Overall Kappa coefficient
1982-1989	0.98	0.97
1990-1999	0.96	0.95
2000-2009	0.98	0.97
2010-2019	0.99	0.99

3.2. Land use/Land cover detection analysis

According to land cover classification ([Figure 2](#)), the bare soil class covers most of the territory of Iraq. Bare soil is distributed on the west and north-west of the study area. The trend of bare soil started to decrease from

1982 to 2019. The northern part of the study area was dominated by vegetation, while in the central and south of the study area are a combination of dense vegetation, built-up and water body.

Figure 2 and Table 2 illustrate the changes in LULC proportions over the examined periods. Bare soil area was changed from 17,584, 41,588, 50,753 and 61,296 Km² in the P1, P2, P3, and P4, respectively. From P1 to P4 it decreased by 8.4%. The trend observed the built-up class increased dramatically by 248.6% from 17,584 km² in 1982 to 61,296 km² in 2019. While, the trends observed in vegetation proportion follow the opposite direction; vegetation increased from 40,414 in P1 to 69,098 km² in P2, while the trends observed decreased to 37,496 km² in P3 and 32,264 km² in P4. Overall, from P1 to P2 vegetation class decreased by 20.2%. Waterbody coverage decreased from the first three decades from 9,596 to 3,983 km², however, the trend was increased through the last decade to arrive 7,111 km². The water bodies in the study area include rivers, lakes and irrigation water.

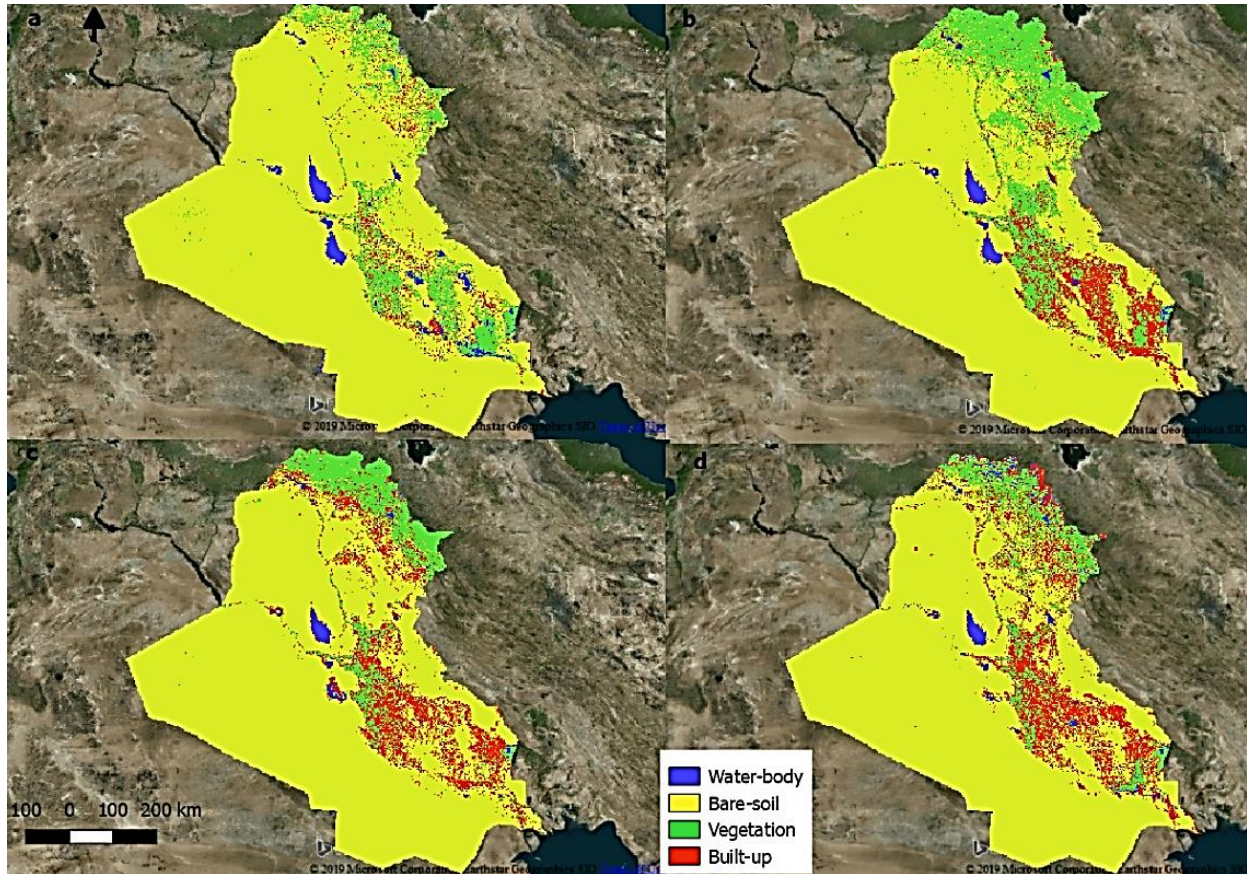


Figure 2. Land Use Land Cover Change. a: period 1982-1989, b: 1990-1999, c: 2000-2009, d: 2010-2019

Table 2. LULC classes change from period 1982_1989 to 2010_2019

Classes	P1: 1982-1989		P2: 1990-1999		P3: 2000-2009		P4: 2010-2019		Changes from P1 and P4	
	%	Area (Km ²)	%	Area (Km ²)	%	Area (Km ²)	%	Area (Km ²)	%	Area (Km ²)
Built-up	4.1	17,584	9.6	41,588	11.8	50,753	14.2	61,296	248.6	43,712
Water body	2.2	9,596	1.3	5,682	0.9	3,983	1.6	7,111	-25.9	-2,485
Bare-soil	84.2	360,977	73.0	315,067	78.6	339,202	76.7	330,765	-8.4	-30,212
Vegetation	9.4	40,414	16.0	69,098	8.7	37,496	7.5	32,264	-20.2	-8,151

The geographical distribution of different LULC classes was demonstrated in the four periods. The ratio between areas of land cover was utilized at different decades to illustrate land cover changes as demonstrated in Table 2. The main conversion to Built-up area occurred from Vegetation and Bare soil classes. From P1, P2, P3 and P4 the Built-up increased dramatically from 4.1, 9.6, and 11.8 to 14.2% respectively (Figure 3). This conversion is natural when we making a comparison between the populations of Iraq from 1984 to 2019. The population of Iraq increased 172.37% in the same period based on Worldometer's elaboration of the latest United Nations data. This increase in the population has already caused urban growth. Most bare soil in Iraq is a desert area. The conversion of bare soil areas into a built-up area has been reduced this class over time. In particular, Bare soil class decreased from 84.2 in P1 to 76.7% in P4.

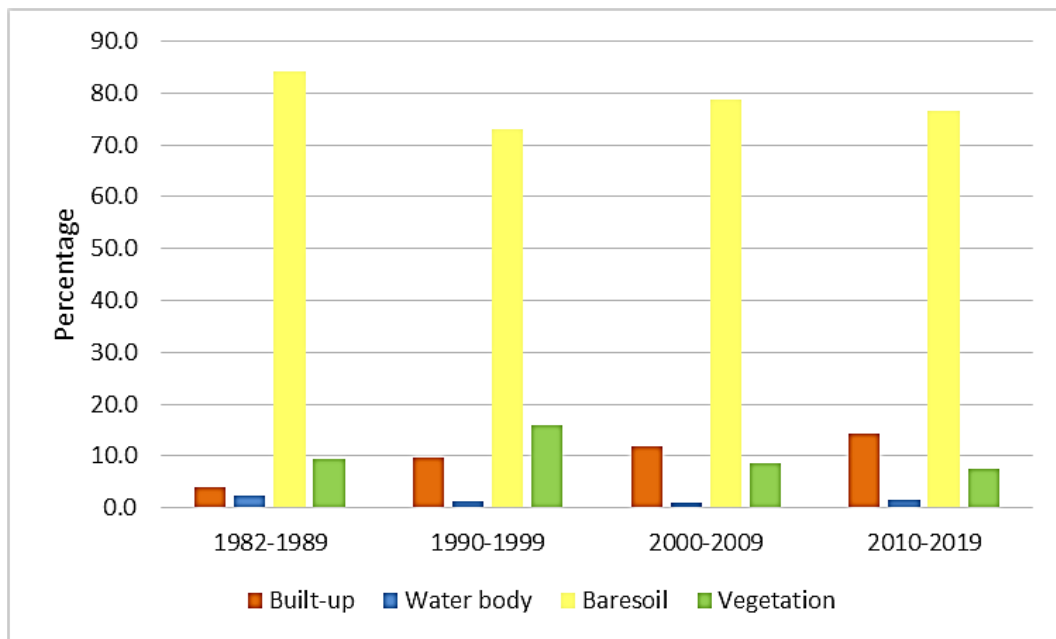


Figure 3. Land use land cover change in Iraq from 1982 to 2019 (%)

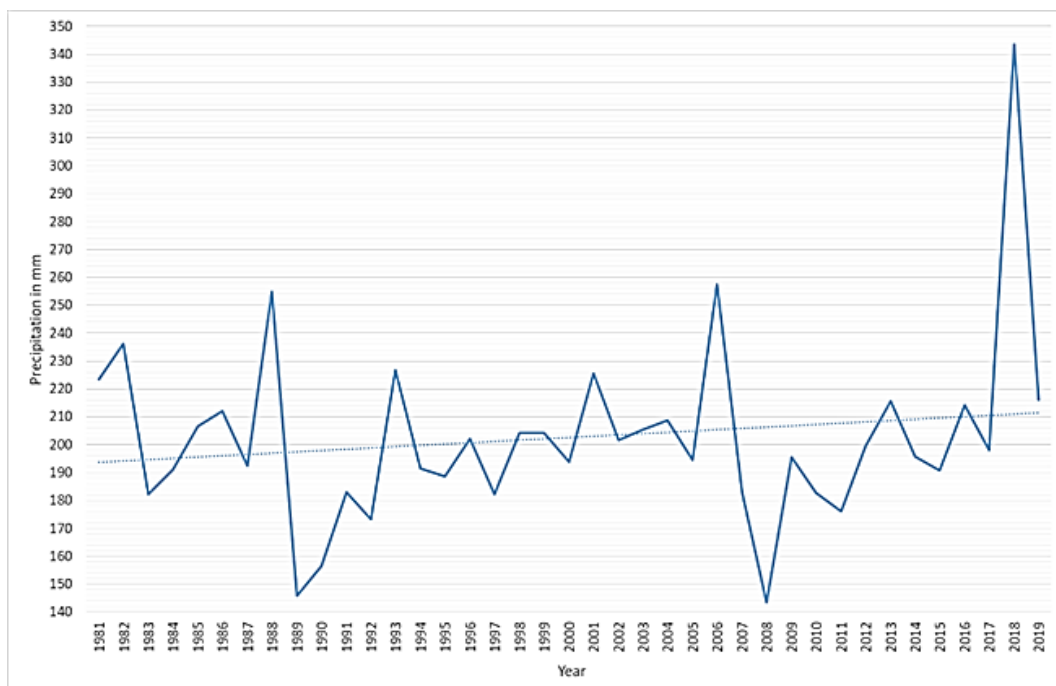


Figure 4. Trend of precipitation in Iraq from 1981 to 2019 based on Climate Hazards Group Infrared Precipitation with Station Data [49]

Vegetation cover was observed more density in the north part of the study area. The vegetation of the study area consists of agriculture, forest, pasture and grass areas. Most distribution of vegetation depends on the fed-rain. Therefore, there is a relationship between annual precipitation and the increase or decrease amount of vegetation in the study area. Figure 4 and Table 3 illustrate the trend of rainfall in the study area from 1981 to 2019. The trend of precipitation increased from P1 to P2. This change in the trend of rainfall effect on the amount of vegetation in the same period. Vegetation cover was increased from 9.4 to 16.0% from P1 to P2 which is associated with the same period of rainfall increasing, while vegetation cover was decreased by 8.7 to 7.5% from P3 to P4. Trend rainfall changes effect directly on the amount of vegetation distribution. There are several factors that additionally impact on vegetation such as wildfire and many political and economic crises that assist to land cover degradation such as Iraq and Iran war from 1980 to 1988, the economic blockade against Iraq from 1991 to 2003, poor state administration. Especially, in central and southern of the country has been leading to breakdown land cover management after 2003.

Table 3. Precipitation in Iraq from 1981 to 2019 based on climate hazards group infrared precipitation with station data

Year	Precipitation (mm)	Year	Precipitation (mm)	Year	Precipitation (mm)	Year	Precipitation (mm)
1981	222	1991	182	2001	224	2011	175
1982	235	1992	172	2002	201	2012	198
1983	181	1993	225	2003	204	2013	214
1984	190	1994	191	2004	208	2014	195
1985	205	1995	188	2005	194	2015	190
1986	211	1996	201	2006	256	2016	213
1987	191	1997	182	2007	182	2017	197
1988	253	1998	203	2008	143	2018	342
1989	145	1999	204	2009	194	2019	271
1990	156	2000	193	2010	182		

4. Conclusion

Investigation four decades of LULC change in Iraq demonstrated how classes converted besides population growth and environmental changes. Nowadays, LULC detection is a crucial indicator of environmental change because it is associated with the climate, ecosystem procedures, land degradation, biodiversity and increased human actions. The objective of current research is to observe how the main LULC class changed in Iraq from 1982 to 2019. Overall, in the study, 5259 Landsat 4, 5 and 8 images were utilized for land classification. We performed Random Forest classifier method in Google Earth Engine (GEE) platform.

Our result achieved 95% and higher accuracy assessment of both overall accuracy and kappa coefficient of four periods. The trend of classes demonstrates that bare soil which covers most territories of Iraq decreased by 8.4% (30,212 km²) from 1982-1989 to 2010-2019. Moreover, vegetation class decreased by 20.2% (8,151 km²) during the same period. In contrast, built up class increased dramatically by 248.6% (43,712 km²). In the future, more research should be done to effectively treat the negative side effects of conversion vegetation and bare soil classes to build up areas in Iraq.

Funding

This research received no external funding.

Author contributions:

Azad Rasul: Conceptualization, Methodology, Software, Visualization, Writing-Reviewing and Editing. **Hasan Hameed:** Writing-Original draft preparation, Writing-Reviewing and Editing. **Gaylan Faqe Ibrahim:** Writing-Original draft preparation, Writing-Reviewing and Editing.

Conflicts of interest

The authors declare no conflicts of interest.

References

- Ganasri, B.P., & Dwarakish. G.S. (2015). Study of Land Use/Land Cover Dynamics through Classification Algorithms for Harangi Catchment Area, Karnataka State, INDIA. *Aquatic Procedia*, 4,1413-1420. <http://doi.org/10.1016/j.aqpro.2015.02.183>
- Xiao, J, Shen, Y., Ge, J., Tateishi, R., Tang, C., Liang, Y., & Huang, Z. (2006). Evaluating Urban Expansion and Land Use Change in Shijiazhuang, China, by Using GIS and Remote Sensing. *Landscape and Urban Planning* 75 (1-2): 69-80. <http://doi.org/10.1016/j.landurbplan.2004.12.005>.
- Friedl, M. A., Sulla-Menashe, D., Tan, B., Schneider, A., Ramankutty, N., Sibley, A., & Huang, X. (2010). MODIS Collection 5 Global Land Cover: Algorithm Refinements and Characterization of New Datasets. *Remote Sensing of Environment* 114 (1). Elsevier Inc.: 168-182. <http://doi.org/10.1016/j.rse.2009.08.016>.
- Hameed, H. M., Faqe, G. R., & Rasul, A. (2020). Effects of land cover change on surface runoff using GIS and remote sensing: a case study Duhok sub-basin. In *Environmental Remote Sensing and GIS in Iraq* (pp. 205-223). Springer, Cham. http://doi.org/10.1007/978-3-030-21344-2_9.
- Usman, M., Liedl, R., Shahid, M. A., & Abbas, A. (2015). Land use/land cover classification and its change detection using multi-temporal MODIS NDVI data. *Journal of Geographical sciences*, 25(12), 1479-1506. <http://doi.org/10.1007/s11442-015-1247-y>.

6. Buyadi, S. N. A., Mohd, W. M. N. W., & Misni, A. (2013). Impact of land use changes on the surface temperature distribution of area surrounding the National Botanic Garden, Shah Alam. *Procedia-Social and Behavioral Sciences*, 101, 516-525.
7. Roy, S., Farzana, K., Papia, M., & Hasan, M. (2015). Monitoring and Prediction of Land Use/Land Cover Change Using the Integration of Markov Chain Model and Cellular Automation in the Southeastern Tertiary Hilly Area of Bangladesh. *International Journal of Sciences:Basic and Applied Researchs* 24 (October): 125–148.
8. Hamad, R., Balzter, H., & Kolo, K. (2018). Predicting Land Use/Land Cover Changes Using a CA-Markov Model under Two Different Scenarios. *Sustainability (Switzerland)* 10 (10): 1–23. <http://doi.org/10.3390/su10103421>.
9. Liu, D., Zhua, Q., & Li, Y. (2016). Land Cover Change Detection in Chinese Zhejiang Province Based on Object-Oriented Approach. *Earth Resources and Environmental Remote Sensing/GIS Applications VII* 10005: 100051J. <http://doi.org/10.1117/12.2241175>.
10. Pai, B. J., & Shenoy, K. N. (2015). Land Use Land Cover Pattern in the Vicinity of Mannapalla Lake, Manipal. *Aquatic Procedia* 4 (Icwrcoe). Elsevier B.V.: 1405–1412. <http://doi.org/10.1016/j.aqpro.2015.02.182>.
11. Long, H., Tang, G., Li, X., & Heilig, G. K. (2007). Socio-Economic Driving Forces of Land-Use Change in Kunshan, the Yangtze River Delta Economic Area of China. *Journal of Environmental Management* 83 (3): 351–364. <http://doi.org/10.1016/j.jenvman.2006.04.003>.
12. Figueiredo, J., & Pereira, H. M. (2011). Regime Shifts in a Socio-Ecological Model of Farmland Abandonment. *Landscape Ecology* 26 (5): 737–749. <http://doi.org/10.1007/s10980-011-9605-3>.
13. Weng, Q. (2001). A Remote Sensing?GIS Evaluation of Urban Expansion and Its Impact on Surface Temperature in the Zhujiang Delta, China. *International Journal of Remote Sensing*, 22 (10): 1999–2014. <http://doi.org/10.1080/713860788>.
14. Chen, S., Zeng, S., & Xie, C. (2000). Remote sensing and GIS for urban growth analysis in China. *Photogrammetric Engineering and Remote Sensing*, 66(5), 593-598.
15. Gislason, P. O., Benediktsson, J. A., & Sveinsson, J. R. (2006). Random forests for land cover classification. *Pattern recognition letters*, 27(4), 294-300.
16. Mahdianpari, M., Salehi, B., Mohammadimanesh, F., & Motagh, M. (2017). Random forest wetland classification using ALOS-2 L-band, RADARSAT-2 C-band, and TerraSAR-X imagery. *ISPRS Journal of Photogrammetry and Remote Sensing*, 130, 13-31.
17. Mahdianpari, M., Salehi, B., Mohammadimanesh, F., Homayouni, S., & Gill, E. (2019). The first wetland inventory map of newfoundland at a spatial resolution of 10 m using sentinel-1 and sentinel-2 data on the google earth engine cloud computing platform. *Remote Sensing*, 11(1), 43.
18. Thanh Noi, P., & Kappas, M. (2018). Comparison of random forest, k-nearest neighbor, and support vector machine classifiers for land cover classification using Sentinel-2 imagery. *Sensors*, 18(1), 18.
19. Whyte, A., Ferentinos, K. P., & Petropoulos, G. P. (2018). A new synergistic approach for monitoring wetlands using Sentinels-1 and 2 data with object-based machine learning algorithms. *Environmental Modelling & Software*, 104, 40-54.
20. Jadcowski, M. A., Howard, R. R., & Brostuen, D. E. (1990). Application of SPOT data for regional growth analysis and local planning [J]. *Photogrammetric engineering and remote sensing*, 56(2), 175-180.
21. Othman, A. A., Shihab, A. T., Al-Maamar, A. F., & Al-Saady, Y. I. (2020). Monitoring of the land cover changes in Iraq. In *Environmental Remote Sensing and GIS in Iraq* (pp. 181-203). Springer, Cham. http://doi.org/10.1007/978-3-030-21344-2_8.
22. Araya, Y. H., & Cabral, P. (2010). Analysis and modeling of urban land cover change in Setúbal and Sesimbra, Portugal. *Remote Sensing*, 2(6), 1549-1563. <http://doi.org/10.3390/rs2061549>.
23. Mitsova, D., Shuster, W., & Wang, X. (2011). A cellular automata model of land cover change to integrate urban growth with open space conservation. *Landscape and urban planning*, 99(2), 141-153. <http://doi.org/10.1016/j.landurbplan.2010.10.001>.
24. Peijun, D. U., Xingli, L. I., Wen, C. A. O., Yan, L. U. O., & Zhang, H. (2010). Monitoring urban land cover and vegetation change by multi-temporal remote sensing information. *Mining Science and Technology (China)*, 20(6), 922-932. [http://doi.org/10.1016/S1674-5264\(09\)60308-2](http://doi.org/10.1016/S1674-5264(09)60308-2).
25. Dewan, A. M., & Yamaguchi, Y. (2009). Land use and land cover change in Greater Dhaka, Bangladesh: Using remote sensing to promote sustainable urbanization. *Applied geography*, 29(3), 390-401. <http://doi.org/10.1016/j.apgeog.2008.12.005>.
26. Hegazy, I. R., & Kaloop, M. R. (2015). Monitoring urban growth and land use change detection with GIS and remote sensing techniques in Daqahlia governorate Egypt. *International Journal of Sustainable Built Environment*, 4(1), 117-124. <http://doi.org/10.1016/j.ijbs.2015.02.005>.
27. Quarmby, N. A., & Cushnie, J. L. (1989). Monitoring urban land cover changes at the urban fringe from SPOT HRV imagery in south-east England. *International Journal of Remote Sensing*, 10(6), 953-963.
28. López, E., Bocco, G., Mendoza, M., & Duhau, E. (2001). Predicting land-cover and land-use change in the urban fringe: A case in Morelia city, Mexico. *Landscape and urban planning*, 55(4), 271-285.

29. Yuan, F., Sawaya, K. E., Loeffelholz, B. C., & Bauer, M. E. (2005). Land cover classification and change analysis of the Twin Cities (Minnesota) Metropolitan Area by multitemporal Landsat remote sensing. *Remote sensing of Environment*, 98(2-3), 317-328.
30. Yin, J., Yin, Z., Zhong, H., Xu, S., Hu, X., Wang, J., & Wu, J. (2011). Monitoring urban expansion and land use/land cover changes of Shanghai metropolitan area during the transitional economy (1979–2009) in China. *Environmental monitoring and assessment*, 177(1), 609-621.
31. Zhang, H., Qi, Z. F., Ye, X. Y., Cai, Y. B., Ma, W. C., & Chen, M. N. (2013). Analysis of land use/land cover change, population shift, and their effects on spatiotemporal patterns of urban heat islands in metropolitan Shanghai, China. *Applied Geography*, 44, 121-133.
32. Mohan, M., & Kandya, A. (2015). Impact of urbanization and land-use/land-cover change on diurnal temperature range: A case study of tropical urban airshed of India using remote sensing data. *Science of the Total Environment*, 506, 453-465.
33. Rasul, A., Balzter, H., & Smith, C. (2016). Diurnal and seasonal variation of surface urban cool and heat islands in the semi-arid city of Erbil, Iraq. *Climate*, 4(3), 42.
34. Yang, L., Xian, G., Klaver, J. M., & Deal, B. (2003). Urban land-cover change detection through sub-pixel imperviousness mapping using remotely sensed data. *Photogrammetric Engineering & Remote Sensing*, 69(9), 1003-1010. <http://doi.org/10.14358/PERS.69.9.1003>.
35. Alberti, M., Weeks, R., & Coe, S. (2004). Urban land-cover change analysis in central Puget Sound. *Photogrammetric Engineering & Remote Sensing*, 70(9), 1043-1052. <http://doi.org/10.14358/PERS.70.9.1043>.
36. Lv, Z. Q., & Zhou, Q. G. (2011). Utility of Landsat image in the study of land cover and land surface temperature change. *Procedia environmental sciences*, 10, 1287-1292. <http://doi.org/10.1016/j.proenv.2011.09.206>.
37. Pal, S., & Ziaul, S. K. (2017). Detection of land use and land cover change and land surface temperature in English Bazar urban centre. *The Egyptian Journal of Remote Sensing and Space Science*, 20(1), 125-145. <http://doi.org/10.1016/j.ejrs.2016.11.003>.
38. Rasul, A., Balzter, H., & Smith, C. (2017). Applying a normalized ratio scale technique to assess influences of urban expansion on land surface temperature of the semi-arid city of Erbil. *International journal of remote sensing*, 38(13), 3960-3980.
39. Ha, T. V., Tuohy, M., Irwin, M., & Tuan, P. V. (2020). Monitoring and mapping rural urbanization and land use changes using Landsat data in the northeast subtropical region of Vietnam. *The Egyptian Journal of Remote Sensing and Space Science*, 23(1), 11-19. <http://doi.org/10.1016/j.ejrs.2018.07.001>.
40. Juliev, M., Pulatov, A., Fuchs, S., & Hübl, J. (2019). Analysis of Land Use Land Cover Change Detection of Bostanlik District, Uzbekistan. *Polish Journal of Environmental Studies*, 28(5), 3235-3242. <http://doi.org/10.15244/pjoes/94216>.
41. Malinowski, J. C. (2002). *Iraq: A Geography*. United States Military Academy, West Point Department of Geography & Environmental Engineering, Building 600, West Point, New York 10996. <https://eric.ed.gov/?id=ED476013>.
42. Metz, H. C. (1990). *Iraq, a Country Study*.
43. Al-Haboby, A., Breisinger, C., Debowicz, D., El-Hakim, A. H., Ferguson, J., van Rheenen, T., & Telleria, R. (2014). *Agriculture for Development in Iraq? Estimating the Impacts of Achieving the Agricultural Targets of the National Development Plan 2013 2017 on Economic Growth, Incomes, and Gender Equality*. Vol. 1349. Intl Food Policy Res Inst.
44. Goldblatt, R., You, W., Hanson, G., & Khandelwal, A. K. (2016). Detecting the boundaries of urban areas in india: A dataset for pixel-based image classification in google earth engine. *Remote Sensing*, 8(8), 634.
45. Breiman, L., & Friedman, J. H. (1985). Estimating optimal transformations for multiple regression and correlation. *Journal of the American statistical Association*, 80(391), 580-598.
46. Kohavi, R. (1995, August). A study of cross-validation and bootstrap for accuracy estimation and model selection. In *Ijcai*, 14(2), 1137-1145.
47. Goldblatt, R., Rivera Ballesteros, A., & Burney, J. (2017). High spatial resolution visual band imagery outperforms medium resolution Spectral imagery for ecosystem assessment in the semi-arid Brazilian Sertão. *Remote Sensing*, 9(12), 1336.
48. Congalton, R. G. (1991). A review of assessing the accuracy of classifications of remotely sensed data. *Remote sensing of environment*, 37(1), 35-46.
49. Funk, C., Peterson, P., Landsfeld, M., Pedreros, D., Verdin, J., Shukla, S., Husak, G., Rowland, J., Harrison, L., Hoell, A., & Michaelsen, J. (2015). The Climate Hazards Infrared Precipitation with Stations—a New Environmental Record for Monitoring Extremes. *Scientific Data*, 2(1), 1-21.





Advanced Remote Sensing

<http://publish.mersin.edu.tr/index.php/arcej>

e-ISSN 2979-9104



Crop classification from multi-temporal PolSAR data with regularized greedy forest

Mustafa Ustuner^{*1} , Fusun Balik Sanli² 

¹Artvin Coruh University, Department of Geomatics Engineering, Artvin, Türkiye, mustuner@artvin.edu.tr

²Yildiz Technical University, Department of Geomatics Engineering, Istanbul, Türkiye, fbalik@yildiz.edu.tr

Cite this study: Ustuner, M., & Sanli, F. B. (2021). Crop classification from multi-temporal PolSAR data with regularized greedy forest. *Advanced Remote Sensing*, 1(1), 10-15

Keywords

Remote Sensing
Polarimetric SAR
Ensemble Learning
Random Forest
Agriculture

Research Article

Received: 12.11.2021
Revised: 10.12.2021
Accepted: 17.12.2021
Published: 30.12.2021

Abstract

Polarimetric Synthetic Aperture Radar (PolSAR) images are considered as an important data source for the crop mapping and monitoring especially for the time-critical agricultural applications. The objective of this paper is to evaluate the potential of a novel ensemble learning algorithm, Regularized Greedy Forest (RGF), for crop classification from multi-temporal quad-pol PolSAR data. For the classification of crops (maize, potato, wheat, sunflower, and alfalfa) in the study site, the polarimetric features of Cloude-Pottier decomposition (a.k.a H/A/ α decomposition) were used as the input data. The performance of RGF was compared to Random Forests (RF) and Support Vector Machines (SVM) in terms of overall accuracy and Kappa values. Our experimental results demonstrated that RGF can yield higher accuracy (with an overall accuracy of 0.78) than RF and SVM for crop classification using PolSAR images. Moreover, it can be concluded that polarimetric features of Cloude-Pottier decomposition are of efficient for the discrimination of crops using multi-temporal PolSAR data.

1. Introduction

Crop classification is one of the vital and important applications in remote sensing since this information could be used as an input data for crop yield estimation, agricultural planning as well as spatio-temporal monitoring of crops. Spaceborne SAR images are usually preferred for the time-critical agricultural applications because SAR signals are sensitive to the crop structure and dielectric properties. In particular, PolSAR images provide more detailed information for agronomic characteristics as they record the complete characteristics of the scattering in each polarization for the natural targets [1-4].

Polarimetric target decompositions (or target decompositions) are used for easier understanding and simpler interpretation of the complex scattering characteristics of natural and man-made targets [3, 5-7]. In this experimental research, we implemented the Cloude-Pottier decomposition (a.k.a. H/A/ α decomposition) that is a type of eigenvector-based decomposition.

Over the last two decades, a wealth of ensemble learning algorithms has been utilized in remote sensing such as random forests [8], extremely randomized trees [9-10] (a.k.a. extra trees), canonical correlation forest [11-12], extreme gradient boosting (XgBoost) [13], Light Gradient Boosting Machine (LightGBM) [14] and deep forest [15]. We chose Regularized Greedy Forest (RGF) in this experimental research since the regularized greedy forest algorithm has not been fully explored yet for the crop classification using multi-temporal PolSAR data. Furthermore, we compared the classification performance of RGF with the two popular and well-established machine learning algorithms in remote sensing, namely RF and SVM.

In this paper, we consider the following questions. (1) Can RGF yield higher accuracy than RF and SVM for PolSAR image classification in our experimental research? (2) Are polarimetric features of Cloude–Pottier decomposition sufficient for crop discrimination from multi-temporal PolSAR data? The major contributions of our experimental study can be shortly summarized as follows.

(1) We investigated the regularized greedy forest algorithm for the crop classification using the polarimetric features from Cloude–Pottier decomposition.

(2) The performance of RGF in comparison to RF and SVM was evaluated for crop classification from multi-temporal PolSAR images.

The rest of the paper is organized as follows. Section 2 introduces the study area and data. PolSAR data processing and classification models are summarized in Section 3. The details of the experimental results and their discussion are presented in Section 4. And following in Section 5, the final conclusions and some important remarks are provided.

2. Study area and data

In this section, the study area site and the details of the multi-temporal PolSAR dataset will be presented.

2.1. Study area

The study site corresponds to the agricultural fields close the province of Konya, Turkey, illustrated in [Figure 1](#). The region has a flat topography and favorable climate conditions for precision farming. The main crop types covering the study site are alfalfa, maize, potato, summer wheat and sunflower. In-situ data was collected simultaneously at the acquisition dates of the PolSAR images.

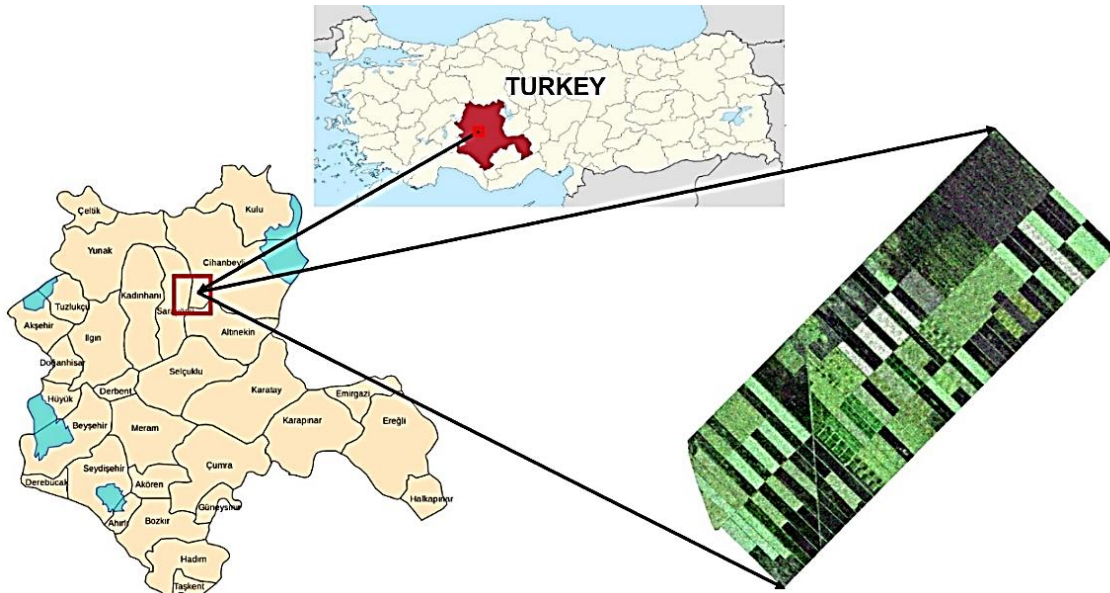


Figure 1. Study area [14]

2.2. Multi-temporal PolSAR dataset

The Multi-temporal quad-polarimetric RADARSAT-2 data (single look complex with fine quad-polarization acquisition mode) was used in our experimental study. The data was acquired for the key dates of the crops as follows: June 13, July 7, July 31 and August 24 of 2016. The data specifications are presented in [Table 1](#).

Table 1. PolSAR Data Specifications

Specifications	Description
Wavelength	C band - 5.6 cm
Resolution (in m)	4.7 x 5.1 (rg x az)
Incidence angle	400
Pass direction	Descending
Acquisition type	Fine quad pol
Polarization	Quad polarimetric
Product type	Single look complex

3. Methods

3.1. PolSAR data processing

Some pre-processing steps for PolSAR data processing are required in order to extract the relevant and proper polarimetric features from target decompositions. In our experimental study, the data pre-processing includes the following steps: (1) data calibration; (2) matrix generation (from coherency matrix); (3) extraction of polarimetric features from Cloude-Pottier decomposition; and (4) orthorectification. All pre-processing steps were implemented using open-source SNAP (The Sentinel Application Platform) v6.0 toolbox, provided by European Space Agency. The data processing steps were illustrated in Figure 2.

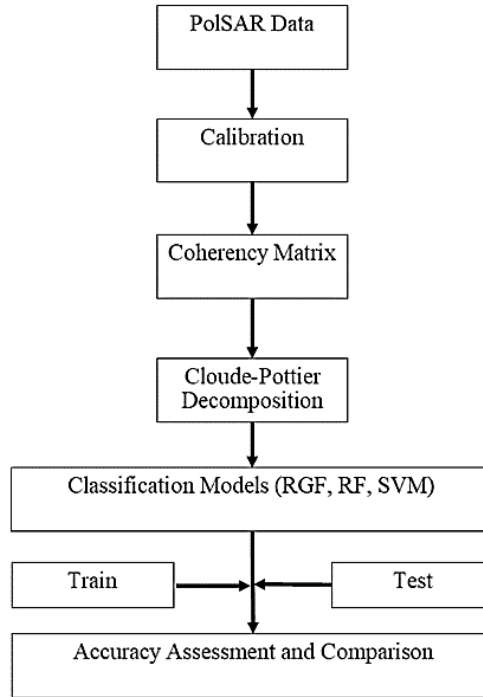


Figure 2. PolSAR Data Processing and Classification

The Cloude-Pottier decomposition (also known as H/A/ α decomposition) is an eigenvector-based decomposition of coherency matrix and separates the total scattering mechanism into three polarimetric features (averaged parameters) which are entropy (H), anisotropy (A) and alpha angle (α). Each feature type provides different information regarding the scattering mechanism such as entropy measures the randomness level of scattering and the alpha angle defines the scattering type of targets (i.e., surface, double-bounce and volume scattering). And the latter parameter, anisotropy, is helpful to demonstrate the differences between the scattering mechanisms [4-5,14,16].

3.2. Image classification

In this experimental study, three different machine learning algorithms were implemented for the crop classification from multi-temporal C-band PolSAR images. The details for training and testing samples were provided in Table 2. The brief summary of the classification models is provided in the following paragraphs.

Table 2. Ground Truth Information

Class	Training	Testing	Total
Alfalfa	1918	3542	5460
Maize	5581	14217	19798
Potato	2275	10604	12879
Sunflower	3729	8915	12644
Wheat	3524	6338	9862

Regularized Greedy Forest (RGF) is a type of tree-based ensemble learning algorithm, developed by [17]. RGF builds decision forests via fully-corrective regularized greedy search by using the underlying forest structure. Fully-corrective regularized greedy search algorithm recursively re-optimizes the coefficients of all decision rules. The novelty of this method is that it combines two ideas: (1) tree-structured regularization into the learning formulation and (2) fully-corrective regularized greedy algorithm. The classification was performed by using the python wrapper of RGF [18].

The Random Forest is one the most frequently used ensemble learning algorithms in remote sensing image classification. RF creates a set of decision trees to make a prediction and the final output of the classifier is determined by the majority voting of the trees [19]. Support Vector Machines are one of the popular kernel-based learning algorithms and based on statistical learning theory. SVM use the kernels to map the data into higher dimensional space for the linear separation of classes. Radial Basis Function kernel was used in our experiment [20-21]. SVM and RF classifications were performed using the open-source Scikit-learn (v 0.19) module in Python v3.6.4 [22].

4. Experimental results and discussion

The classification performance of Regularized Greedy Forest in comparison to RF and SVM was analyzed in our experimental study for the classification of crops from multi-temporal PolSAR data. The overall accuracy of the classified images was derived from the error matrix and the comparison of the methods was assessed in terms of overall accuracy and kappa coefficients. Table 3 presents the overall accuracies and kappa coefficients for the classification algorithms. The highest classification accuracy (overall accuracy of 78.65% and kappa coefficient of 0.72) was produced with RGF while lowest classification accuracy (overall accuracy of 75.08% and kappa coefficient of 0.67) was obtained by SVM. The classified images for each method were presented in Figure 3.

Table 3. Classification Accuracies

Methods	Overall Accuracy (%)	Kappa
SVM	75.08	0.67
RF	76.52	0.69
RGF	78.65	0.72

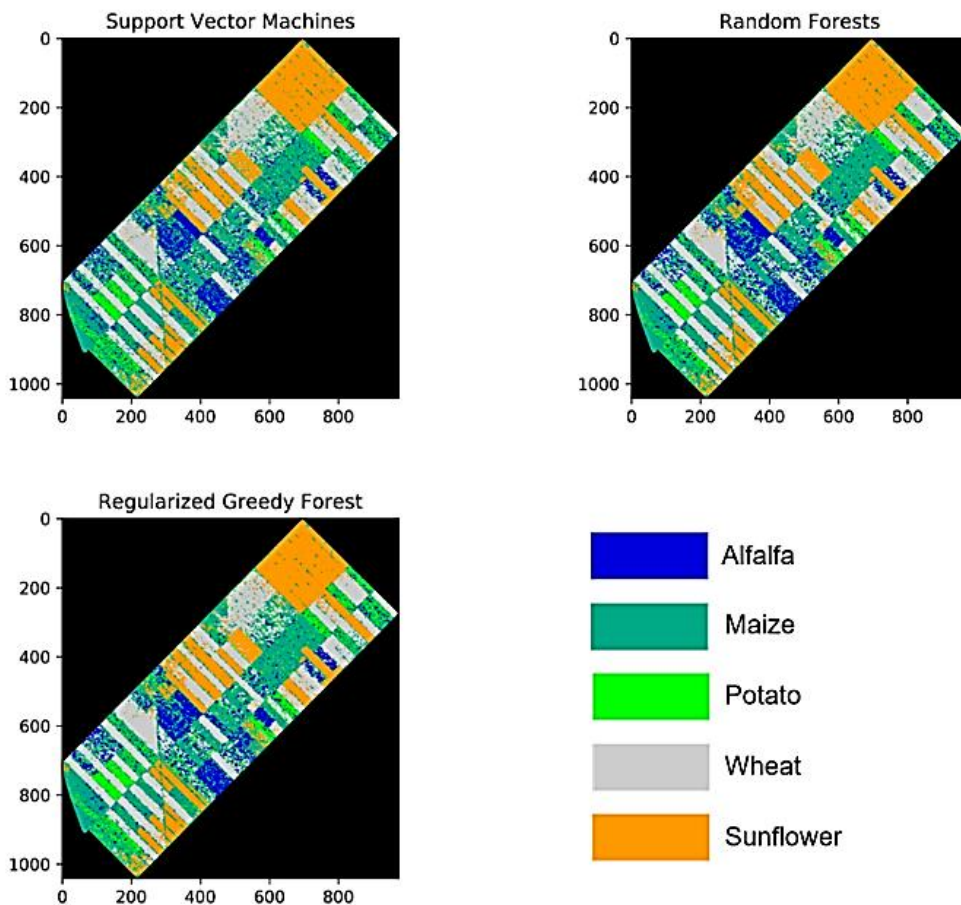


Figure 3. Classified Images

Individual class accuracies were assessed based on F1-score which is the harmonic mean of the user accuracy and producer accuracy values. Table 4 presents the individual class accuracies (based on F1-score) for each classification method.

Table 4. Individual class accuracies (F1-score)

Methods	RGF	RF	SVM
Alfalfa	0.26	0.26	0.28
Maize	0.76	0.74	0.72
Potato	0.70	0.63	0.66
Sunflower	0.99	0.99	0.97
Wheat	0.95	0.95	0.93

Sunflower is the most accurate classified class (0.99) while alfalfa is the least accurate classified class (0.26) in which F1-score could not reach up to the 0.30. SVM predicted the alfalfa class more accurate than other methods though it yielded the lowest classification accuracy. Moreover, SVM obtained higher F1-score than RF for potato and alfalfa classes. Wheat is the second most accurate predicted class in our experimental study where it was predicted above the F-1 score values of 0.90.

5. Conclusion

This research investigated the performance of a novel ensemble learning algorithm, RGF, in comparison to RF and SVM for the crop classification from multi-temporal PolSAR images. The Cloude-Pottier decomposition was implemented for the extraction of the polarimetric features. Our experimental results demonstrated the following conclusions: 1) RGF can yield higher classification accuracy than RF and SVM for the classification of multi-temporal PolSAR images 2) the polarimetric parameters derived from Cloude-Pottier decomposition are suitable for the crop classification. Our future research will focus on the extensive analysis of the polarimetric features derived from incoherent polarimetric decompositions for the crop classification.

Acknowledgement

The authors gratefully acknowledge the data support from TAGEM (Project No: TAGEM/TSKAD/14/A13/P05/03). Mustafa Ustuner received the research fellowship in 2018 by TUBITAK 2214/A International Doctoral Research Fellowship Programme (Grant No #1059B141700579) and would like to thank TUBITAK as well as the Department for Earth Observation of Friedrich-Schiller University of Jena, Germany for hosting him in their department as a guest researcher in 2018.

Author contributions

Mustafa Ustuner: Conceptualization, Methodology, Data curation, Writing-Original draft preparation, Software and Validation. **Fusun Balik Sanli:** Visualization, Investigation, Writing-Reviewing, Editing and Validation

Conflicts of interest

The authors declare no conflicts of interest.

References

1. McNairn, H., & Brisco, B. (2004). The application of C-band polarimetric SAR for agriculture: A review. *Canadian Journal of Remote Sensing*, 30(3), 525-542.
2. Soria-Ruiz, J., Fernandez-Ordóñez, Y., McNairn, H., & Bugden-Storie, J. (2007, July). Corn monitoring and crop yield using optical and RADARSAT-2 images. In *2007 IEEE International Geoscience and Remote Sensing Symposium* (pp. 3655-3658). IEEE.
3. Jiao, X., Kovacs, J. M., Shang, J., McNairn, H., Walters, D., Ma, B., & Geng, X. (2014). Object-oriented crop mapping and monitoring using multi-temporal polarimetric RADARSAT-2 data. *ISPRS Journal of Photogrammetry and Remote Sensing*, 96, 38-46.

4. Tamiminia, H., Homayouni, S., McNairn, H., & Safari, A. (2017). A particle swarm optimized kernel-based clustering method for crop mapping from multi-temporal polarimetric L-band SAR observations. *International Journal of Applied Earth Observation and Geoinformation*, 58, 201-212.
5. Cloude, S. R., & Pottier, E. (1997). An entropy based classification scheme for land applications of polarimetric SAR. *IEEE transactions on geoscience and remote sensing*, 35(1), 68-78.
6. Chen, S. W., Li, Y. Z., Wang, X. S., Xiao, S. P., & Sato, M. (2014). Modeling and interpretation of scattering mechanisms in polarimetric synthetic aperture radar: Advances and perspectives. *IEEE Signal Processing Magazine*, 31(4), 79-89.
7. Steele-Dunne, S. C., McNairn, H., Monsivais-Huertero, A., Judge, J., Liu, P. W., & Papathanassiou, K. (2017). Radar remote sensing of agricultural canopies: A review. *IEEE Journal of Selected Topics in Applied Earth Observations and Remote Sensing*, 10(5), 2249-2273.
8. Pal, M. (2005). Random forest classifier for remote sensing classification. *International Journal of Remote Sensing*, 26(1), 217-222.
9. Barrett, B., Nitze, I., Green, S., & Cawkwell, F. (2014). Assessment of multi-temporal, multi-sensor radar and ancillary spatial data for grasslands monitoring in Ireland using machine learning approaches. *Remote Sensing of Environment*, 152, 109-124.
10. Samat, A., Persello, C., Liu, S., Li, E., Miao, Z., & Abuduwaili, J. (2018). Classification of VHR multispectral images using extratrees and maximally stable extremal region-guided morphological profile. *IEEE Journal of Selected Topics in Applied Earth Observations and Remote Sensing*, 11(9), 3179-3195.
11. Colkesen, I., & Kavzoglu, T. (2017). Ensemble-based canonical correlation forest (CCF) for land use and land cover classification using sentinel-2 and Landsat OLI imagery. *Remote Sensing Letters*, 8(11), 1082-1091.
12. Xia, J., Yokoya, N., & Iwasaki, A. (2016). Hyperspectral image classification with canonical correlation forests. *IEEE Transactions on Geoscience and Remote Sensing*, 55(1), 421-431.
13. Georganos, S., Grippa, T., Vanhuysse, S., Lennert, M., Shmoni, M., & Wolff, E. (2018). Very high resolution object-based land use-land cover urban classification using extreme gradient boosting. *IEEE geoscience and remote sensing letters*, 15(4), 607-611.
14. Ustuner, M., & Balik Sanli, F. (2019). Polarimetric Target Decompositions and Light Gradient Boosting Machine for Crop Classification: A Comparative Evaluation. *ISPRS International Journal of Geo-Information*, 8(2), 97. MDPI AG.
15. Yang, F., Xu, Q., Li, B., & Ji, Y. (2018). Ship detection from thermal remote sensing imagery through region-based deep forest. *IEEE Geoscience and Remote Sensing Letters*, 15(3), 449-453.
16. Cloude, S. R., & Pottier, E. (1996). A review of target decomposition theorems in radar polarimetry. *IEEE Transactions on Geoscience and Remote Sensing*, 34(2), 498-518.
17. Johnson, R., & Zhang, T. (2013). Learning nonlinear functions using regularized greedy forest. *IEEE Transactions on Pattern Analysis and Machine Intelligence*, 36(5), 942-954.
18. RGF Team, "Regularized Greedy Forest (RGF) library" [Online] (2018). Available: <https://github.com/RGF-team/rgf>, 2018. (Accessed on: December. 30, 2019)
19. Gislason, P. O., Benediktsson, J. A., & Sveinsson, J. R. (2006). Random forests for land cover classification. *Pattern Recognition Letters*, 27(4), 294-300.
20. Melgani, F., & Bruzzone, L. (2004). Classification of hyperspectral remote sensing images with support vector machines. *IEEE Transactions on Geoscience and Remote Sensing*, 42(8), 1778-1790.
21. Zeybek, M. (2021). Inlier point preservation in outlier points removed from the ALS point cloud. *Journal of the Indian Society of Remote Sensing*, 49(10), 2347-2363.
22. Pedregosa, F., Varoquaux, G., Gramfort, A., Michel, V., Thirion, B., Grisel, O., ... & Vanderplas, J. (2011). Scikit-learn: Machine learning in Python. *Journal of Machine Learning Research*, 12(Oct), 2825-2830.



© Author(s) 2021. This work is distributed under <https://creativecommons.org/licenses/by-sa/4.0/>



Advanced Remote Sensing

<http://publish.mersin.edu.tr/index.php/arcej>

e-ISSN 2979-9104



Performance analysis of YOLO versions for automatic vehicle detection from UAV images

Melis Uzar*¹, Şennur Öztürk¹, Onur Can Bayrak¹, Tümay Arda¹, Nursu Tunalioglu Öcalan¹

¹Yıldız Technical University, Geomatics Engineering Department, Türkiye, auzar@yildiz.edu.tr, sennurozturk95@gmail.com, onurcb@yildiz.edu.tr, tarda@yildiz.edu.tr, ntunali@yildiz.edu.tr

Cite this study: Uzar, M., Öztürk, Ş., Bayrak, O. C., Arda, T., & Öcalan, N. T. (2021). Performance analysis of YOLO versions for automatic vehicle detection from UAV images. *Advanced Remote Sensing*, 1(1), 16-30

Keywords

UAV
Vehicle detection
YOLO
Deep learning
Remote sensing

Research Article

Received: 14.11.2021
Revised: 11.12.2021
Accepted: 18.12.2021
Published: 30.12.2021

Abstract

Automatic vehicle detection, one of the study areas in Remote Sensing facilities, has become widely used on several issues such as transportation, disaster management, highway management, parking lot management and real-time vehicle detection in smart cities. In recent years, deep learning methods have been widely preferred in vehicle detection. Although this method has advantages such as high accuracy and speed of detection, some problems such as not detecting vehicles, double detection and class confusion in detection from digital images caused by vapor and shadow in adverse weather conditions (i.e., rain, fog, sunlight) have been raised. Thus, vehicle detection is still a significant issue that should be studied. In this study, versions of You Only Look Once (YOLO), one of the deep learning (DL) architectures, have been investigated in terms of performance assessments of vehicle detection in parking lots. To perform the analysis, Unmanned Aerial Vehicle (UAV)-based images collected from Yıldız Technical University, Campus of Davutpasa (dated 2018) were used. The labeling process was performed for three classes (car, bus, and minibus) using the Visual Object Tagging Tool (VoTT). The labeled dataset has been trained via transfer learning in YOLOv4-CSP, YOLOv4-tiny, YOLOv4-P5, YOLOv4-P6, YOLOv5n, YOLOv5s, YOLOv5m, YOLOv5l, YOLOv5x architectures. The weights of YOLO versions have been implemented to the parking lots and results have been compared. To assess the performance of YOLO-based vehicle detection, mAP and F1-Score values were computed.

1. Introduction

Recently, the integration of remote sensing, photogrammetry and deep learning algorithms have obtained fast, real-time, and highly-accurate results. It is obvious that it has opened a new era in various disciplines with technological developments in the fields of deep learning and computer vision. Several object detection studies have been carried out in urban areas. Automatic vehicle detection has become one of the most important topics in the management of highways and parking lots in urban areas, considering the rapidly increasing population and the transportation vehicles that participate in traffic jams.

Cheng et al. [1] carried out a pixel-based classification study for vehicle detection by applying a color filter that separates the colors of vehicles and other objects. The vehicles were identified using the Canny edge detector and classified by Dynamic Bayesian Network (DBN). Chen et al. [2] tackled whether conventional methods are insufficient or not when there is a complex background. They decided to use Deep Neural Networks (DNN) because

of its structure that can learn rich features from the training data. Hence, they presented the Hybrid DNN (HDNN) model by making changes in the pooling layer for the model to detect data at different scales on the DNN. De Almeida et al. [3] introduced a dataset on parking lots and aimed to detect the empty and occupied areas in the parking lot by Support Vector Machines (SVM). In experiments, where the same data was used for both training and testing, accuracy rates of over 99% were achieved. However, when working with different data, the best result was obtained about 89%. In Tan [4], the vehicle dataset consisting of 2000 images of different brands and models was trained with Faster-R-CNN-ResNet 50, Faster-RCNN-ResNet 101, R-FCN-ResNet 101 and SSD-MobileNet using transfer learning. When the results were examined, the Faster RCNN-ResNet 50 model was the most successful with 94%.

Since object detection is a critical part in Automatic Driving Systems (ADS) and Driver Assistance Systems (DAS), current real-time detection models for small vehicle objects suffer from low sensitivity and poor performance. The detection speed of the YOLO algorithm has been of great benefit in the development of automatic driving systems [5-6]. Bui et al. [7] used object detection and tracking models such as YOLO and DeepSort to analyze traffic in complex areas (e.g., intersections). To improve the vehicle counting problem, they propose a zone monitoring approach that can work well with a variety of scenarios, especially in areas with complex movements. The proposed model has been evaluated in the CVPR AI City Challenge 2020 dataset. Accordingly, the method achieved 85% accuracy. Han et al. [8] proposed a new real-time object detection model named YOLOv2, which is optimized based on the YOLOv2 deep learning framework, to be applied to small vehicle objects. In the proposed model, a new structure is introduced to strengthen the feature extraction capability of the network by adding convolution layers to YOLOv2. 94% accuracy was achieved in the model, whose effectiveness was investigated using the open-source dataset KITTI. Wang et al. [9] tested Faster-RCNN, R-FCN, SSD, RetinaNet, and YOLOv3 models using the KITTI dataset. According to the results, R-CNN-type models that work locally in two stages give more accurate results, while the speed of models such as YOLO and SSD.

In this study, the latest versions of YOLO namely YOLOv4 and YOLOv5 were utilized for performance analysis of vehicle detection. Target object classes were aimed as follows: car, minibus and bus. The properties of the study area and the dataset obtained by the UAV system are presented in the next section, followed by an explanation of the methodology adopted. The results of the experiment are reported along with an accuracy assessment of the automatic vehicle detection results with the versions of YOLO deep learning analyses, in the Results and Discussion section, and the conclusion is given in the last section.

2. Material and Method

You Only Look Once (YOLO), which is a deep learning architecture, utilized for the automatic vehicle detection analysis with the data obtained by UAV. The workflow of the proposed methodology is given in Figure 1. In the first stage of automatic on-ground vehicle detection with YOLO architecture, data preparation, i.e., labeling, data augmentation, training, validation and test data split, was made. Model training with transfer learning was used for different versions of YOLO so-called YOLOv4-CSP, YOLOv4-tiny, YOLOv4-P5, YOLOv4-P6, YOLOv5s, YOLOv5l, YOLOv5m, YOLOv5n and YOLOv5x. The performance analysis of target classes (car, minibus and bus) was evaluated with nine YOLO versions and then accuracy and performance analyses were performed. In this study, Roboflow software was used for data augmentation processes using UAV images. The labeling processes of the target classes were created using Visual Object Tagging Tool (VoTT) software. Mean Average Precision (mAP), F1-Score, precision and recall parameters were computed for performance analysis of YOLO versions for vehicle detection.

2.1. Study area and dataset

In this study, parking lots located at Davutpasa Campus of Yildiz Technical University in Istanbul, Turkey were selected as regions of interest (RoI) (Figure 2). The aerial images were collected with the UAV system in 2018. Figure 3 shows samples from RoI including parking lots. Totally 94 images were obtained with a size of 5472 * 3648 pixels and a resolution of 72 dpi.

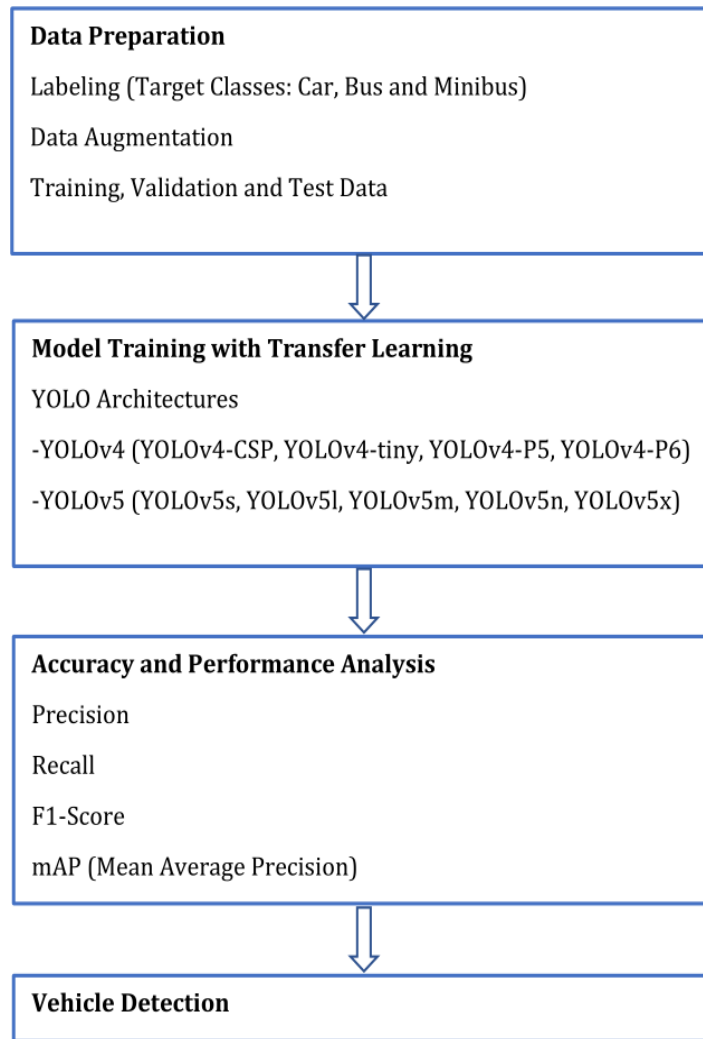


Figure 1. Workflow of vehicle detection

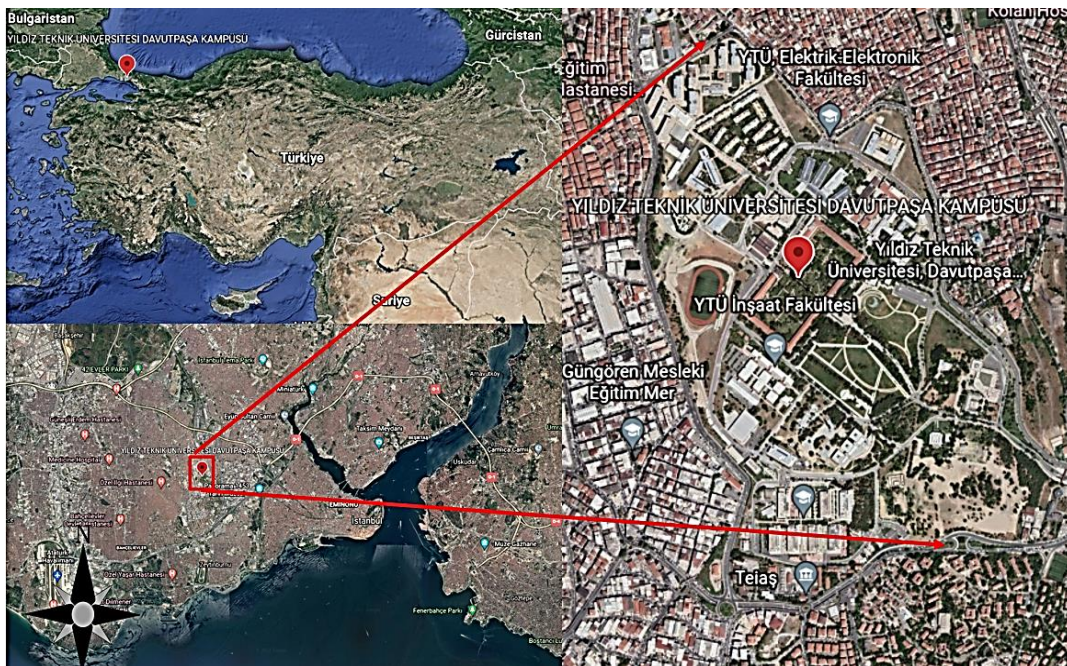


Figure 2. Study area

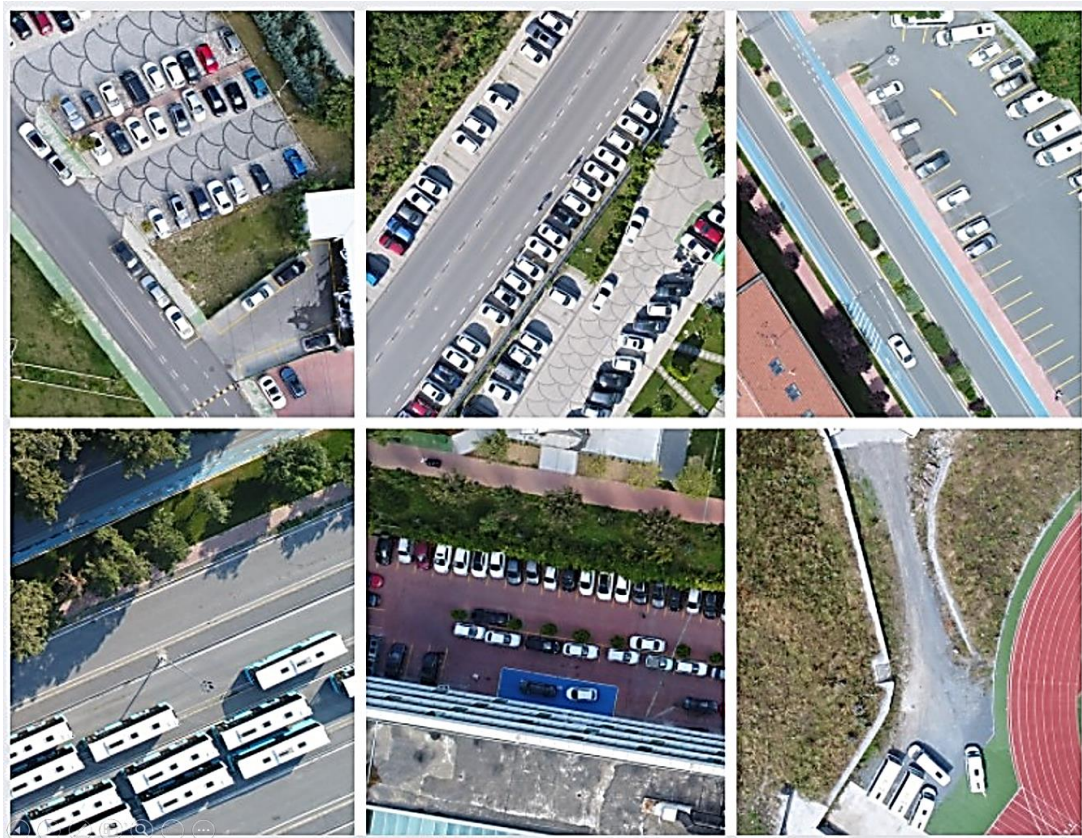


Figure 3. Some samples of parking lots from RoI

2.2. Data preparation

Data preparation phase was carried out in 3 main stages as (1) labeling, (2) data augmentation, and (3) training, validation and test data split.

2.2.1. Labelling

Data labeling is a process that transforms data into a descriptive format for artificial intelligence (AI) applications. Generating the desired output in AI-based models is highly dependent on accurate and well-labeled data. Labeled data should be reliable, accurate and consistent. Features that do not belong to any target class should not be labeled. The required number of labels should be made in the data and the data for each label should be sufficiently various.

2.2.2. Data augmentation

Data augmentation is a technique, which is commonly used to train large neural networks by increasing the diversity of the data without collecting new samples. This transformation technic is closely related to digital image processing in data analysis, which used to augment images in deep learning. In most of the studies, the data augmentation techniques are applied to the dataset to contribute to the representative ability of the dataset. In this study we utilized the fundamental three methods of data augmentation as follows; brightness analysis, shear and rotation. Brightness analysis is used to change the brightness of the image. After this technique the result image becomes darker or lighter than the original one. The process of shear transformation, which is to fix the one axis and stretch the image at a certain angle known as the shear angle. The image is rotated randomly by an angle in the range of (+) value to (-) value in the rotation process. The samples of brightness, shear and rotation images from study were given in [Figure 4](#).

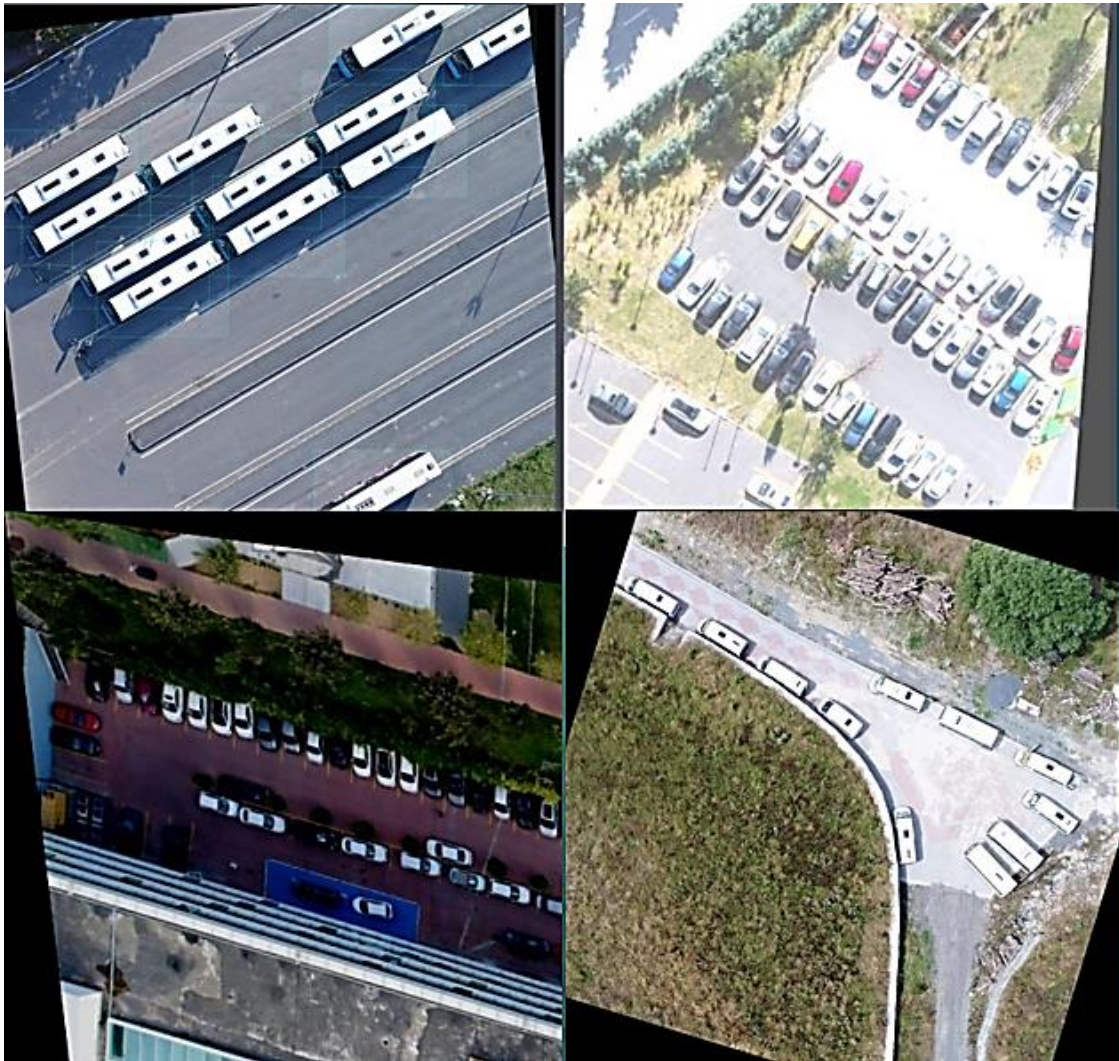


Figure 4. The samples of brightness, shear and rotation images

2.2.3. Training, validation and test data

One of the important issues of machine learning is the generalization of the developed model. Generalization is an indicator representing the performance and fitness of the model for new data. Data are separated into training, validation and test dataset to measure generalization. Training, validation and test data have a strong relation on fitness of model (Figure 5). Training dataset is a sample of data used to fit the model during the learning process. Training data determines the parameters of the model. The validation dataset is used to provide an unbiased evaluation of a model fit on the training dataset while tuning the hyperparameter. The evaluation process of the validation data is to determine the hyperparameter values for the model. Test data is the part of the dataset used to assess the final fit of the model performance.



Figure 5. Splitting the train, validation and test dataset

2.3. Model Training with Transfer Learning for YOLO Architectures

2.3.1 Transfer learning

Re-training a model on a new task that was pre-trained for another task is known as transfer learning. In order to train complex models, the dataset must be large enough and representative of the real situation. Generally, most remote sensing-based transfer learning works are focused on updating the weights of a deep learning solution from another context to the current task based on available training data [10]. However, previously trained dataset

is often used to take advantage of the time and expert knowledge. Transfer learning is valuable for data science because it reduces the need for large amounts of data. Using transfer learning instead of end-to-end learning provides better performance with less data and less training time. Hence, the use of MS COCO dataset, which includes 2.5 million labeled samples of 91 objects in 328,000 images was preferred. In addition, selection of this dataset's pre-trained models is appropriate since it covers car, bus, and minibus classes.

2.3.2. YOLO Architectures

In this study, the latest versions of YOLO namely YOLOv4 and YOLOv5 were used for performance analysis of vehicle detection. The YOLOv4 model was developed with Cross Stage Partial (CSP) structure [11]. This model is configured as backbone, neck and head. Backbone is the layer of the feature extraction process, which is added as a middle layer to find more features while estimating objects. YOLOv4 uses Spatial Attention Module (SAM), Path Aggregation Network (PAN) and spatial pyramid pooling (SPP) instead of Feature Pyramid Network (FPN). At head, there are bounding boxes and the estimated boxes of each class. In literature, there are versions of YOLOv4 namely YOLOv4-CSP, YOLOv4-tiny, YOLOv4-P5, YOLOv4-P6 and YOLOv4-P7. The Scaled YOLOv4 model was developed by [12], which has the YOLOv4 object detection neural network based on the CSP approach scaled up and down (Figure 6). This model is adaptable to all network structures while maintaining optimum speed and accuracy. The CSP layer, which was added to the YOLO architecture, has a simple structure and offers very efficient results. In this structure, half of the data produces semantic information as it moves along the line, while the other half is added to the model later, preserving both spatial information and some properties. Scaled YOLOv4 changes not only the depth, width, resolution of the mesh, but also its structure. After the scaled YOLOv4 model, the YOLOv4-tiny model was developed for low-capacity GPUs. The YOLOv4-tiny model has different considerations from the scaled YOLOv4 model because different constraints such as memory bandwidth and memory access are considered in it. The backbone structure of the YOLOv4-tiny model uses OSANet, which offers favorable computational complexity at small depth. After the YOLOv4-tiny model, the YOLOv4-Large model was developed for high-capacity GPUs and scaled from P5 to P7. In this model, as the scale increases along with the depth and width of the model, the complexity of the structure also increases. The depth scale is given as 1, 3, 15, 15, 7, 7 and 7 from small model to large model at each stage, respectively.

The YOLOv5 model was introduced by Glenn Jocher after the release of YOLOv4. The generalized structure of the YOLOv5 model is given in Figure 7. In this model, as in the YOLO v4 model, CSPNet backbone and PANet neck are used. Likewise, the same structure of the model in YOLOv4 is used in the head part of YOLOv5. The difference between YOLOv5 versions (YOLOv5n, YOLOv5s, YOLOv5m, YOLOv5l and YOLOv5x) is the scaling factors of the width and depth of the mesh (Figure 8). In Table 1, the number of layers, parameter numbers and performance information about the versions are given.

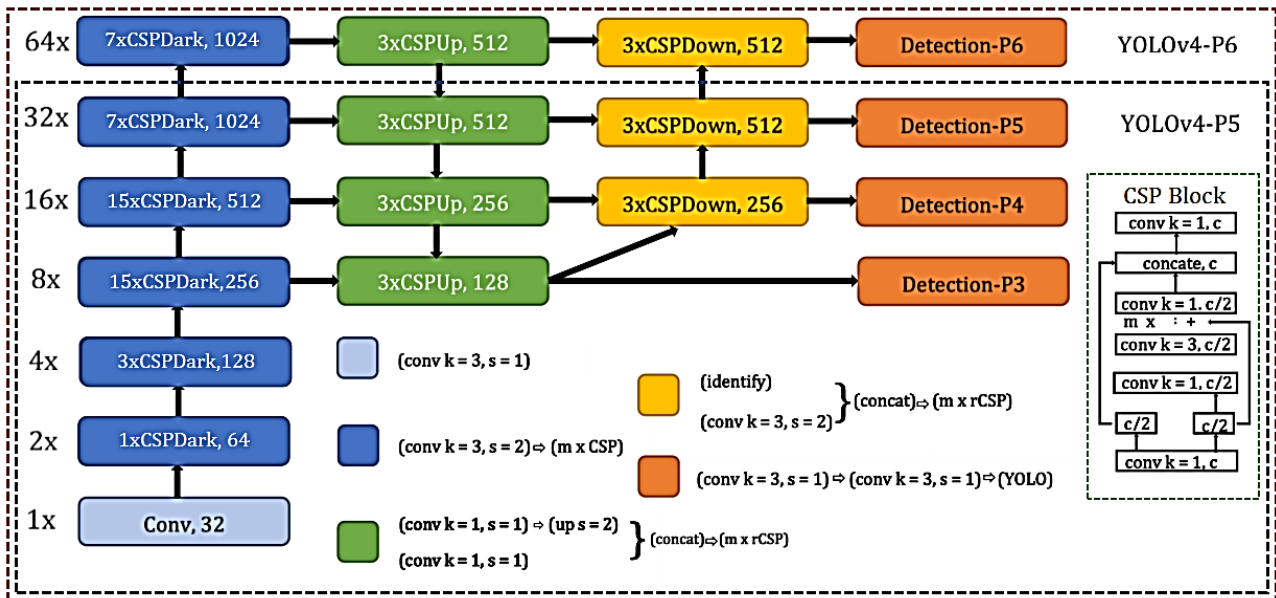


Figure 6. Scaled YOLOv4 layer architecture [12]

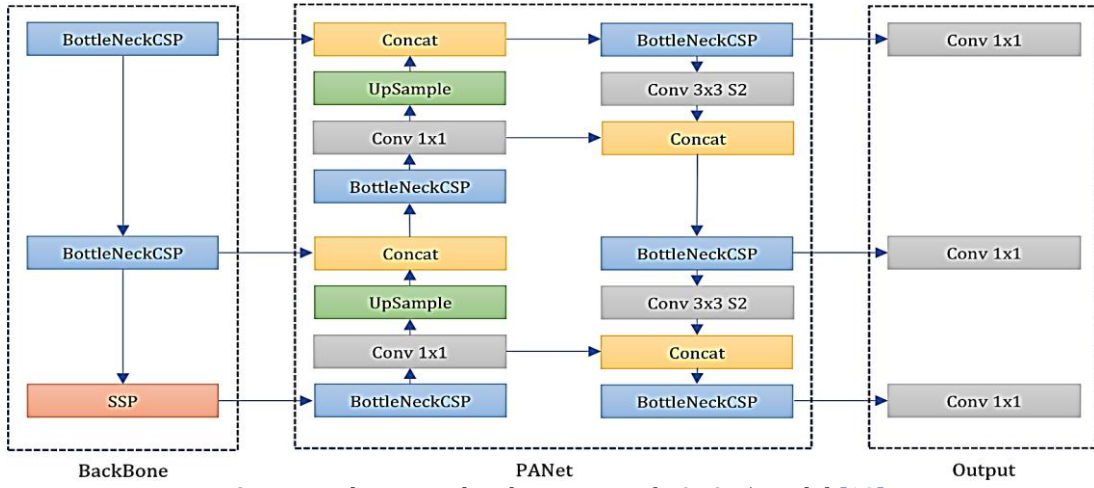


Figure 7. The generalized structure of YOLOv5 model [13]

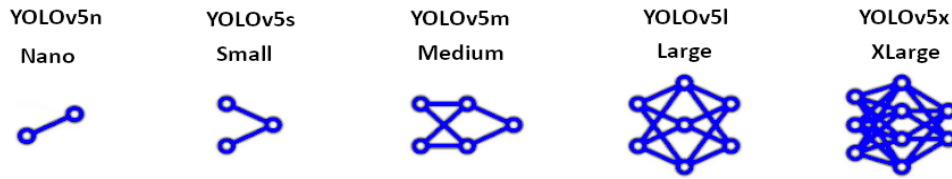


Figure 8. Scales of YOLOv5

Table 1. Specifications of YOLOv5 models

Model	Number of Layers	Number of Parameters	FLOPs
YOLOv5n	270	1.767.976	4.2
YOLOv5s	270	7.027.720	15.9
YOLOv5m	369	20.879.400	48.1
YOLOv5l	468	46.149.064	108.0
YOLOv5x	567	86.231.272	204.2

2.4. Accuracy and performance analysis

To assess the performance of YOLO-based vehicle detection, mAP and F1-Score values were computed. Actual annotations were compared with predictions according to confusion matrix (Table 2).

Table 2. Confusion Matrix

Confusion Matrix		Actual	
		Positive	Negative
Predicted	Positive	TP (True Positive)	FP (False Positive)
	Negative	FN (False Negative)	TN (True Negative)

Moreover, some performance metrics are given below in (Eq.1-5);

$$\text{Precision} = \frac{TP}{TP + FP} \quad (1)$$

$$\text{Recall} = \frac{TP}{TP + FN} \quad (2)$$

$$\text{F1 - Score} = \frac{2}{\left(\frac{1}{\text{Precision}}\right) + \left(\frac{1}{\text{Recall}}\right)} \quad (3)$$

$$\text{AP} = \sum_{k=0}^{k=n-1} [\text{Recall}(k) - \text{Recall}(k + 1)] * \text{Precision}(k) \quad (4)$$

$$\text{mAP} = \frac{1}{n} \sum_{k=1}^{k=n} \text{AP}_k \quad (5)$$

where, AP and mAP are the average and mean average precisions; n is the number of classes and AP_k is the AP value of the related class (k).

3. Results

3.1. Data preparation

Before the data preparation process, pre-processes were applied to ensure the availability and suitability of the aerial images of the study area with the YOLO architecture and to increase the accuracy. At this stage, the images were cropped as the dimensions of 2048 x 2048 pixels. In the data preparation process, the images were labeled in three classes: car, bus and minibus, which were vehicles on campus parking lots. There are 1223 labels of car, 122 labels of minibus and 54 labels of bus in the dataset. After this step, data augmentation was performed, followed by the dataset split process utilized as 75%, 15%, and 10% of training, validation and test, respectively. The values of ± 10 brightness, 15-degree vertical shear, and $\pm 15, 25, \text{ and } 90$ -degree rotation were applied in data augmentation.

3.2 YOLO model training

In the training process, the pre-trained weights of the MS COCO dataset were accepted as the initial weights and imported into YOLO architectures. The hyperparameters of the YOLOv4-CSP, YOLOv4-tiny, YOLOv4-P5, YOLOv4-P6, YOLOv5n, YOLOv5s, YOLOv5m, YOLOv5l and YOLOv5x models for training were given in [Table 3](#).

Table 3. The hyperparameter values used in training

Hyperparameters	Values
Batch Size	16
Input Size	416 x 416
Momentum	Momentum: 0.937 Initial Learning Size: 0.01
Epoch Size	200
Activation Function	YOLOv4: Mish; YOLOv5: Leaky ReLU
Optimization Algorithm	ADAM

3.3 Accuracy Analysis of Model Training

In this study, nine different YOLO versions were trained and [Table 4](#) includes the results of the accuracy analyses of trained models. Analyses were performed by comparing metrics computed between actuals and predictions.

Table 4. Training metrics of trained models (fps refers to frame per second)

MODEL	Precision	Recall	F1-Score	mAP	fps
YOLOv4-CSP	0.61	0.78	0.68	0.76	11
YOLOv4-tiny	0.86	0.91	0.89	0.75	63
YOLOv4-P5	0.47	0.86	0.61	0.73	9
YOLOv4-P6	0.38	0.89	0.53	0.75	8
YOLOv5n	0.77	0.80	0.79	0.82	63
YOLOv5s	0.85	0.78	0.81	0.80	40
YOLOv5m	0.8	0.78	0.79	0.84	25
YOLOv5l	0.84	0.75	0.79	0.79	12
YOLOv5x	0.87	0.74	0.80	0.79	10

According to [Table 4](#), the YOLOv4-tiny model provides the F1-Score of 0.89 as the highest value. Although YOLOv5 models perform similar results, it is seen that YOLOv4-CSP, YOLOv4-P5, YOLOv4-P6 models offer relatively lower F1-Scores compared to the other architectures. Additionally, all of the YOLOv5 models perform higher mAP values than YOLOv4 models. The YOLOv5m provides the mAP of 84% as the highest value. In order to perform real-time vehicle detection, the fps values of the models were considered and compared. In [Table 4](#), it is seen that YOLOv4-tiny and YOLOv5n models with a processing speed of 63 fps are the fastest ones, which are

developed for low-performance systems. The slowest models are YOLOv4-P5, YOLOv4-P6 and YOLOv5x that are developed for high performance systems.

As seen from Table 4, all of the YOLOv5 models provided the highest mAP values. Thus, mAP results regarding the classes i.e., car, minibus, and bus were analyzed for the YOLOv5 models. Table 5 represents the mAP results regarding the classes i.e., car, minibus, and bus for YOLOv5 models. The results show that cars are the most accurately detected class in all models. According to the table, the classes of minibus and bus reduce the overall accuracy. In Figure 9, detection results of target classes; minibus, bus and car for YOLOv5, in Figure 10 the sample display of results for cars and in Figure 11 the sample detection results of target classes; minibus, bus and car are given.

Table 5. The mAP analysis for classes

Model	Car	Minibus	Bus
YOLOv5n	0,94	0,80	0,60
YOLOv5s	0,82	0,73	0,77
YOLOv5m	0,90	0,73	0,74
YOLOv5l	0,94	0,82	0,66
YOLOv5x	0,93	0,82	0,61

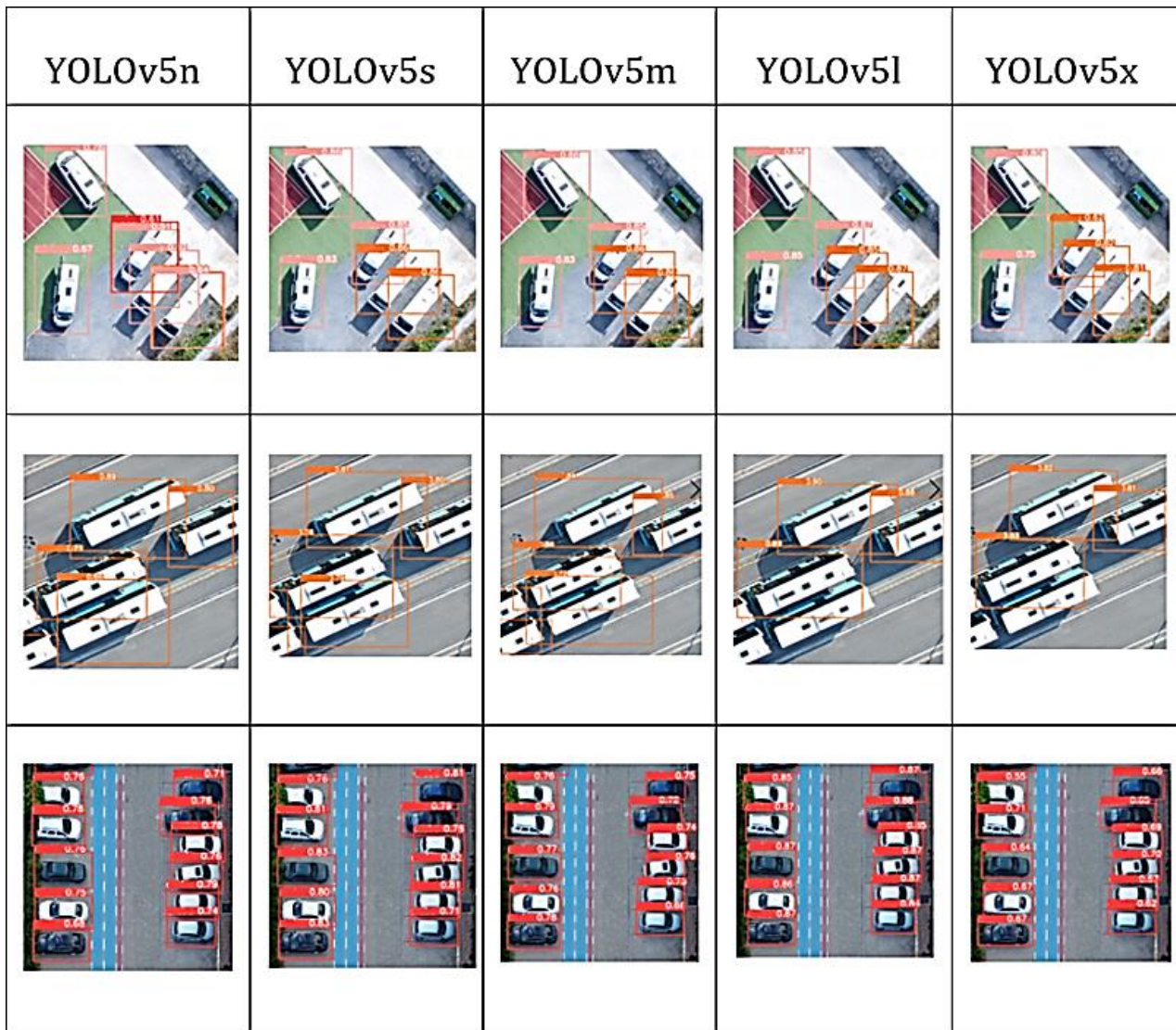


Figure 9. Detection results of target classes; minibus, bus and car for YOLOv5



Figure 10. The sample display of results for cars



Figure 11. The sample display of results from target classes

4. Discussion

YOLO versions were preferred to perform the performance analysis of vehicle detection in terms of speed, accuracy, and learning capabilities. The YOLO model improves the speed of detection due to its working structure as in real-time. This model requires only a single forward propagation through a neural network to detect vehicles and also use a single bounding box regression to estimate the height, width, center, and target class of vehicles. YOLO is a prediction technique that provides accurate results with minimum errors. The architecture of YOLO has a learning capability for vehicle detection that enables it to learn the representations of vehicles.

According to the results, the highest accuracy value for F1-Score was provided by the YOLOv4-tiny model with 89% among all of the YOLO models in detecting vehicles in parking lots. Moreover, all of the YOLOv5 models present accuracies in the range of 79%-81%. Nevertheless, the accuracies of YOLOv4-CSP, YOLOv4-P5 and YOLOv4-P6 models were found below 70%. According to the mAP criteria, preferred widely in the literature to perform detection performance, the best accuracy value was obtained in the YOLOv5m model with 84%. For the other YOLOv5 models, the lowest mAP value was 79% and for all of the YOLOv4 models, mAP values were in the range of 73%-76%. According to the mAP results, an accuracy value of over 82% was obtained for car class in all of the models. The overall accuracy reduced depending on bus and minibus classes. There are a low number of buses and minibus in the training dataset, because the study area was restricted by the campus boundaries.

In this study, another significant factor for selecting YOLO models in vehicle detection is the speed of detection. Labeling time of 94 images with a size of 2048 x 2048 took 5 hours. While model training in a cloud environment with the support of Google-Colaboratory GPU took approximately 2 hours for models with low depth, for the models with higher depth and complexity, that took about 7 hours. The total training duration for 9 models was about 40 hours. When the YOLO models were evaluated in terms of speed, it is seen that the speed results were provided directly proportional to the increase in scale. The fastest models are YOLOv5n and YOLOv4-tiny models with 63 fps. The YOLOv5s model with a speed of 40 fps and YOLOv5m model with a speed of 25 fps showed a performance close to the small-scale models. The detection speeds of the other models were in the range of 8-12 fps.

As a result, the advantages and disadvantages of different YOLO model versions were compared within the scope of vehicle detection and their performances were analyzed in this study. YOLOv4 and YOLOv5, which are the two advanced models of the YOLO architecture so far, have been preferred because of the detection success in accuracy. For this purpose, the most common problems; black vehicle detection, vehicle shadow detection, non-vehicle object detection, detection of vehicles covered by trees and not being able to detect vehicles were analyzed for YOLOv4 and YOLOv5 models.

In the model performance analysis, the correctly captured vehicle is shown with a frame in all of the figures. First, it was observed that there were incorrect or missing vehicle detection in the images obtained when trees covered the vehicles (Figure 12). Secondly, an important factor affecting the vehicle detection accuracy of the models is the errors due to shadows (Figure 13). Thirdly, in some YOLO models as shown in Figure 14 and Figure 15, vehicles were not detected correctly when dark colored vehicles such as black and gray glow under the

influence of sunlight and have the same pixel gray value as the road object. Another important problem is that inaccurate vehicle detections caused by non-vehicle objects with the same geometric and color characteristics as the vehicle have been observed. Sidewalk (Figure 16) and container (Figure 17) could be given as an example of non-vehicle object detection. One of the important reasons for this situation is that the model was not trained well enough. In other words, as a result of insufficient labeling of different objects, the model cannot learn the properties of the objects and detects the target classes incomplete or incorrectly.

It is seen that the color texture of the vehicles in the image has the same reflection value as the road, due to the fact that dark colored vehicles such as black and gray shine with the effect of sunlight. For this reason, the detection of road and vehicle objects according to the working principle and weight parameters in the structures of some YOLO models has not been carried out correctly. On the other hand, non-vehicle object detection problems have occurred in YOLOv4-CSP, YOLOv4-tiny, YOLOv4-P5, YOLOv4-P6, YOLOv5l, YOLOv5x models. Considering this problem, it has been observed that objects with similar geometry and close-image gray values to the training data labeled as vehicles are detected as vehicles incorrectly. On the other hand, in the YOLOv5n, YOLOv5s, and YOLOv5m models among all of the models, accurate vehicle detection has been achieved in containers, sidewalk and road objects, which have the same gray values as the bus.

5. Conclusion

In this study, the YOLO model, one of the commonly used object detection architectures in deep learning, was implemented for performance analysis of automatic vehicle detection using UAV-based aerial images within the scope of YTU Davutpasa Campus parking lots. For the performance analysis of vehicle detection, 9 different versions of the YOLO models namely YOLOv4-CSP, YOLOv4-tiny, YOLOv4-P5, YOLOv4-P6, YOLOv5s, YOLOv5l, YOLOv5m, YOLOv5n, YOLOv5x were utilized. Firstly, the data preparation stage, including labeling, data augmentation, training, validation and test data split, were performed. Secondly, model training with transfer learning was carried out for YOLO versions. At the training stage, the weights trained with the MS COCO dataset were accepted as initial weights and included in the deep learning network using transfer learning. The car, minibus and bus were labeled as target classes. A confusion matrix was created for the target classes and the results were compared in terms of mAP, recall, precision, and F1-Score values. In addition, the accuracy analysis and speed comparisons of the models were considered. At the last stage, the weights trained were applied to the test data containing the parking lots.

According to the results, when analyzing the dataset with a limited GPU support, it is seen that large-scale models could not be trained properly. Thus, to determine the real performances of YOLOv4-P5, YOLOv4-P6, YOLOv5l and YOLOv5x models, it is recommended to train models with an unlimited GPU support and more training epochs. Moreover, the number and diversity of the dataset should be increased with the use of high-capacity processors.

In recent years, integration of remote sensing and photogrammetry with deep learning methods will provide significant solutions especially in automatic object detection and extraction in terms of high accuracy, speed, and real-time data processing. In particular, this integration will be a very important data source for local and private administrations such as for the management of smart cities with accurate and real-time vehicle detection, planning at roads and intersections, and management of transportation. In deep learning algorithms, transferring the features of objects to the model as parameter values with different weights using training networks and image processing techniques will become the most preferred method of obtaining data information in the future. Today, where accurate data is the most valuable information, it can be concluded that object classes belonging to roads and road networks will be supportive for the management and planning of highways and parking lots thanks to large data processing and integration with geographic information systems.

Funding

This research received no external funding.

Author contributions

Melis Uzar: Conceptualization, Methodology, Writing-Original draft preparation, **Şennur Öztürk:** Methodology, Software, Data curation, **Onur Can Bayrak:** Investigation, Software, Data curation, **Tümay ARDA:** Visualization, Validation, **Nursu Tunalioğlu Öcalan:** Methodology, Writing-Reviewing and Editing.

Conflicts of interest

The authors declare no conflicts of interest.

YOLOv4-CSP	YOLOv4-tiny	YOLOv4-P5	YOLOv4-P6	
				
YOLOv5n	YOLOv5s	YOLOv5m	YOLOv5l	YOLOv5x
				

Figure 12. The effect of trees on vehicle detection










YOLOv4-CSP	YOLOv4-tiny	YOLOv4-P5	YOLOv4-P6	
				
YOLOv5n	YOLOv5s	YOLOv5m	YOLOv5l	YOLOv5x
				

Figure 13. The effect of shadows in the image on vehicle detection

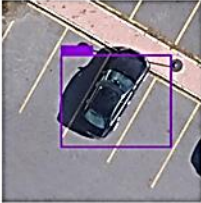

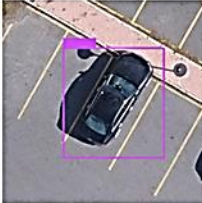






YOLOv4-CSP	YOLOv4-tiny	YOLOv4-P5	YOLOv4-P6	
				
YOLOv5n	YOLOv5s	YOLOv5m	YOLOv5l	YOLOv5x
				

Figure 14. The incorrect detection sample for the black colored vehicle in YOLOv4-P6










YOLOv4-CSP	YOLOv4-tiny	YOLOv4-P5	YOLOv4-P6	
				
YOLOv5n	YOLOv5s	YOLOv5m	YOLOv5l	YOLOv5x
				

Figure 15. The performance of YOLOv4 and YOLOv5 for the black colored vehicle detection










YOLOv4-CSP	YOLOv4-tiny	YOLOv4-P5	YOLOv4-P6	
				
YOLOv5n	YOLOv5s	YOLOv5m	YOLOv5l	YOLOv5x
				

Figure 16. Non-vehicle object detection: sidewalk example

YOLOv4-CSP	YOLOv4-tiny	YOLOv4-P5	YOLOv4-P6	
				
YOLOv5n	YOLOv5s	YOLOv5m	YOLOv5l	YOLOv5x
				

Figure 17. Non-vehicle object detection: container example

References

1. Cheng, H.Y., Weng, C. C., & Chen, Y. Y. (2011). Vehicle detection in aerial surveillance using Dynamic Bayesian Networks. *IEEE Transactions on Image Processing*, 21(4), 2152-2159.
2. Chen, X., Xiang, S., Liu, C. L., & Pan, C.H. (2014). Vehicle detection in satellite images by Hybrid Deep Convolutional Neural Networks. *IEEE Geoscience and remote sensing letters*, 11(10), 1797-1801.
3. De Almeida, P.R., Oliveira, L.S., Britto Jr, A.S., Silva Jr, E.J. & Koerich, A.L. (2015). PKLot–A Robust dataset for parking lot classification. *Expert Systems with Applications*, 42(11), 4937-4949.
4. Tan, Z. (2019). Vehicle classification with deep learning. Master's thesis, Firat University, Institute of Science, Elazığ, 63p.
5. Ataei, B. (2019). Development of video processing algorithm (YOLO) in autonomous vessels operations. Master's Thesis, University of South-Eastern Norway, 64p
6. Peng, B., Keskin, M. F., Kulcsár, B. & Wymeersch, H. (2021). Connected autonomous vehicles for improving mixed traffic efficiency in unsignalized intersections with deep reinforcement learning. *Communications in Transportation Research*, 1, 100017.
7. Bui, N., Yi, H. & Cho, J. (2020). A vehicle counts by class framework using distinguished regions tracking at multiple intersections. In *Proceedings of the IEEE/CVF Conference on Computer Vision and Pattern Recognition Workshops*, 578-579, Seattle, WA, USA.
8. Han, X., Chang, J. & Wang, K. (2021). Real-Time object detection based on YOLO-V2 for tiny vehicle object. *Procedia Computer Science*, 183, 61-72.
9. Wang, H., Yu, Y., Cai, Y., Chen, X., Chen, L. & Liu, Q. (2019). A comparative study of state-of-the-art deep learning algorithms for vehicle detection. *IEEE Intelligent Transportation Systems Magazine*, 11(2), 82-95.
10. Benbahria, Z., Sebari, I., Hajji, H. & Smiej, M. F. (2021). Intelligent mapping of irrigated areas from Landsat 8 images using transfer learning. *International Journal of Engineering and Geosciences*, 6(1), 40-50.
11. Bochkovskiy, A., Wang, C. Y. & Liao, H. Y. M. (2020). YOLOv4: Optimal speed and accuracy of object detection. *arXiv preprint arXiv:2004.10934*.
12. Wang, C. Y., Bochkovskiy, A. & Liao, H. Y. M. (2021). Scaled-YOLOv4: Scaling cross stage partial network. In *Proceedings of the IEEE/cvf Conference on Computer Vision and Pattern Recognition*, 13029-13038.
13. URL-1, (2020). <https://github.com/ultralytics/yolov5/issues/280>, [18.02.2022]



© Author(s) 2021. This work is distributed under <https://creativecommons.org/licenses/by-sa/4.0/>



Advanced Remote Sensing

<http://publish.mersin.edu.tr/index.php/arcej>

e-ISSN 2979-9104



Evaluation of the relationship between urban area and land surface temperature determined from optical satellite data: A case of Istanbul

Gülcan Sarp*¹, Emre Baydoğan ¹, Firdevs Güzel ¹, Tuğba Otlukaya ¹

¹Suleyman Demirel University, Department of Geography, Türkiye, gulcansarp@sdu.edu.tr, emrebay07@gmail.com, firdevsguzel3@gmail.com, tgbkocabas@gmail.com

Cite this study: Sarp, G., Baydoğan, E., Güzel, F., & Otlukaya, T. (2021). Evaluation of the relationship between urban area and land surface temperature determined from optical satellite data: A case of Istanbul. *Advanced Remote Sensing*, 1(1), 31-37

Keywords

Land Surface
Temperature
Normalized Building
Difference Index
Landsat 8 OLI-TIRS

Research Article

Received: 16.11.2021
Revised: 12.12.2021
Accepted: 19.12.2021
Published: 30.12.2021

Abstract

In recent years, the formation of urban heat islands occurring both depending on urban structuring and human activities has been the focus of attention of many researchers. In particular, remote sensing data has been widely used in this type of research. Because with the development in satellite and remote sensing technologies, satellite sensors that detect at different spatial, spectral, and radiometric resolutions not only enable the determination of land use classes on the Earth's surface but also allow the determination of the land surface temperature. In this study, Landsat 8 OLI-TIRS images of 2018 were used to determine the urban area and land surface temperature. Urban areas were determined by applying Normalized Building Difference Index (NDBI) to the Short-Wave Infrared (SWIR) and Near Infrared (NIR) bands of the Landsat 8 OLI sensor. Thermal Infrared (TIR) bands of the Landsat 8 TIRS sensor were used to determine the land surface temperature (LST). According to the results obtained, the lowest average temperature value is 22 °C in the Adalar district and the highest average temperature value is 33 °C in the Gaziosmanpaşa district, and there is a positive 76% linear relationship between the urban object ratio and the land surface temperature.

1. Introduction

It is known that urban areas with dense impermeable surfaces such as buildings or roads have an impact on climate at different scales. Therefore, urban areas tend to offer a higher temperature compared to the surrounding rural areas.

Today, the increasing availability of images from Landsat series satellites on a global scale has enabled both periodic and high spatial resolution analysis of the relationship between urban growth dynamics and land surface temperature. To make this comparison correctly, first of all, it is necessary to determine the urban areas from satellite images with high spatial accuracy. For this purpose, different algorithms designed to determine urban areas with high spatial accuracy have been proposed in the literature. Some of those; Urban Index (UI) [1], Bare soil index (BI) [2], Normalized Difference Bareness Index (NDBaI) [3], Index-based building index (IBI) developed to determine the characteristics of built-up areas from satellite images [4], and Enhanced Built-Up and Bareness Index (EBBI) developed to map built-up and bare land in an urban and urban area [5], have been employed in various studies. These indices are widely adopted for monitoring urban growth, given their relative simplicity and easy implementation. The basis of these algorithms is that urban areas have a higher reflection response in the short wavelength infrared (SWIR) wavelength range of the Electromagnetic spectrum compared to green, red, and, near-infrared (NIR) ranges.

Land Surface Temperature (LST) is widely used in hydrology, meteorology, geography, urban heat islands, forest fires, hydrological modeling on a regional and global scale [6-7]. In studies conducted to determine land surface temperature and urban heat island formations. With the developments in remote sensing technologies, satellite sensors that detect in the thermal infrared region of the electromagnetic spectrum are used as an information source for determining the surface temperature. Landsat series satellites of them are often preferred among researchers because they have sensors that shoot in the Thermal Infrared (TIR) region. Taha [8] determined the causes and effects of the formation of urban heat islands. Jiang and Tian [9], on the other hand, investigated the effects of land change and land use on land surface temperature using the thermal bands of Landsat ETM+ satellite imagery. Bokaie et al. [10] evaluated the urban heat island in Tehran based on the relationship between land use and land surface temperature. Sarp [11] investigated the relation between LST and vegetation relation based on Landsat TM5 data and found a significant inverse relationship between the LST and vegetation. Erener and Sarp [12] evaluated the environmental effects of the dams in their study and tested the relationship between vegetation, surface humidity, and surface temperature distributions in these areas statistically. Sarp et al. [13] evaluated industrialization effects on urbanization and urban heat island formation and found a strong relationship between industrialization, urbanization, and heat island formation. Zhang et al. [14] evaluated the changes in LST of the Ebinur lake between 1998 and 2011 and stated that the Landsat image is valuable data to estimate the relationship between LST and land cover factors. Temurçin et al. [15] evaluated the urban heat island formations through the structural differences in the morphology of the Istanbul city. In the study, they observed that the urban heat island effects increase in areas with high building density in the horizontal and vertical directions and that the urban heat island values increase by 1-2 °C in areas where the vertical structuring is intense compared to the surrounding areas.

In this study, the relationship between land surface temperature and urban areas obtained from Landsat 8 OLI (Operational Land Imager) and TIRS (Thermal Infrared Sensor) satellite images were tried to be evaluated for the province of Istanbul. The difference of this study from previous studies is the use of images from the same satellite in determining both urban areas and land surface temperature, as well as a statistical comparison of urban object density and land surface temperature values on a district basis.

2. Material and Method

The image of the Landsat 8 OLI-TIRS satellite was used in the study, dated April 23, 2018, was downloaded free of charge from the United States Geological Survey (USGS) website [16]. Landsat 8 satellite has 2 sensors, OLI and TIRS. This satellite receives images in the Visible, Near Infrared (NIR), Short Wave Infrared (SWIR) and Thermal Infrared (TIR) ranges and has a spatial resolution of between 15 and 100 meters depending on the spectral range [7]. The technical specifications of the Landsat 8 OLI- TIRS satellite are given in Table 1 [7].

Table 1. Technical Specifications of Landsat 8 OLITIRS satellite

Bands	Spectral Range (micrometers)	Resolutions (m)
Band 1 Coastal Aerosol	0.43 - 0.45	30
Band 2 Blue	0.45 - 0.51	30
Band 3 Green	0.53 - 0.59	30
Band 4 Red	0.64 - 0.67	30
Band 5 Near InfraRed	0.85 - 0.88	30
Band 6 Short Wave Infrared (SWIR1)	1.57 - 1.65	30
Band 7 Short Wave Infrared (SWIR2)	2.11 - 2.29	30
Band 8 Panchromatic	0.50 - 0.68	15
Band 9 Cirrus	1.36 - 1.38	30
Band 10 Thermal Infrared	10.60-11.19	100
Band 11 Thermal Infrared	11.50 - 12.51	100

The method of the study consists of four different stages. In the first stage, Normalized Building Difference Index (NDBI) was obtained from the SWIR and NIR bands of the Landsat 8 OLI sensor, and the Normalized Vegetation Difference Index (NDVI) was obtained from the NIR and R bands of the Landsat 8 OLI sensor. In the second stage, NDBI and NDVI imageries are converted to binary classes with the help of natural breaks Jenks algorithm. In the third stage, the Land Surface Temperature (LST) was obtained from the TIR (band 10) of the Landsat 8 TIRS sensor. In the last stage, the relationship between the urban object ratios in each district area and the LST was evaluated with the Pearson linear correlation.

2.1. Normalized Difference Built-Up Index (NDBI)

For the identification of urban areas from Landsat 8 OLI-TIRS satellite images, Normalized Building Difference Index (NDBI) proposed by Zha et al. [17] was used. The main purpose of developing this index is to highlight urban areas with higher reflectance in the short-wave infrared (SWIR) region and lower in the near-infrared (NIR) region. NDBI is calculated using the Equation 1.

$$NDBI = \frac{(SWIR - NIR)}{(SWIR + NIR)} \quad (1)$$

In the resulting image (Figure 1a), NDBI values vary between -1 and +1, values close to +1 correspond to areas with urban objects (buildings, roads, etc.), while values close to -1 correspond to green areas and soil areas where there is no settlement.

Since only urban objects are dealt with in this study, NDBI results are converted into binary classes representing residential areas (1) and other areas (0) with the natural breaks Jenks algorithm (Figure 1b). In the resulting image, residential areas representing urban objects could be determined up to 30 m in spatial resolution provided by Landsat 8 OLI satellite.

To determine the urban object ratio on a district basis, the urban object ratios were calculated by districts, taking into account the number of values represented by 0 and 1 within each district boundary (Table 2). According to the results obtained, the districts with the highest rate of urban objects are Güngören with 52%, Gaziosmanpaşa with 45%, and Şişli with 42%. The districts with the lowest rate of urban objects are Şile with 2%, Çekmeköy, Adalar, and Beykoz districts with 3%.

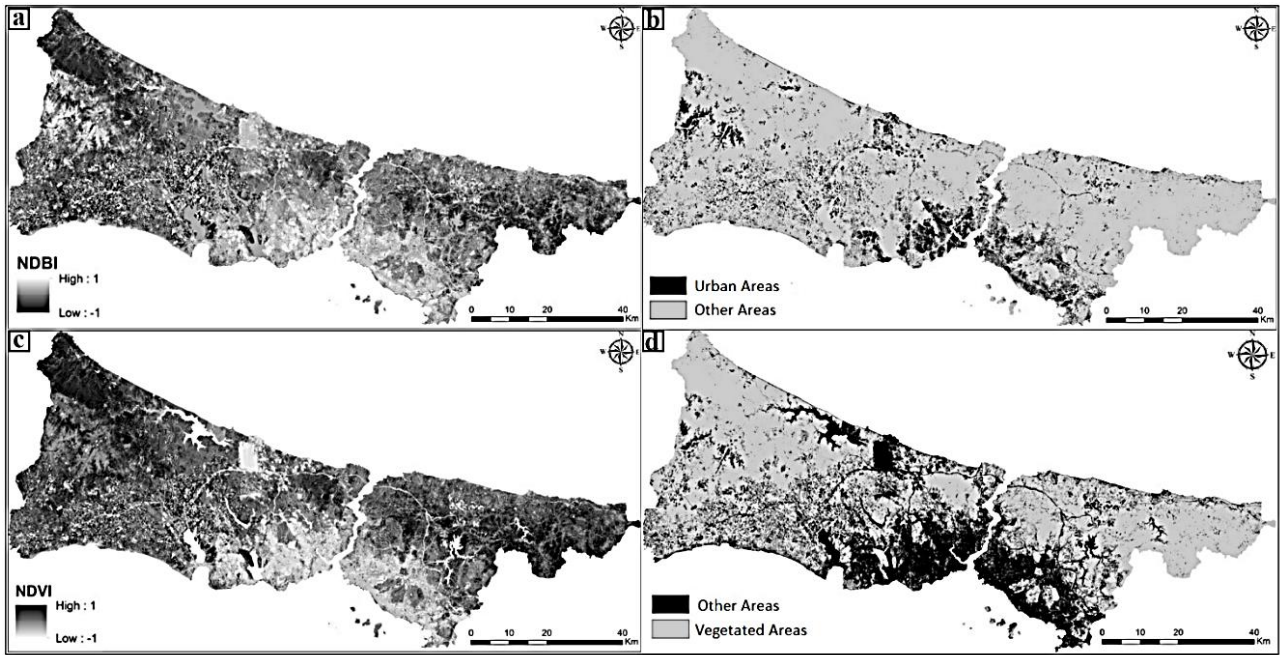


Figure 1. Normalized Building Difference Index (NDBI) Result (a); The result of the Jenks algorithm applied to the NDBI (0 (other areas) and 1 (urban areas)) (b); Normalized Difference Vegetation Index (NDVI) Result (c); The result of the Jenks algorithm applied to the NDVI (0 (other areas) and 1 (vegetated areas)) (d).

Table 2. Urban object ratios by districts

District Name	Building Density by Districts (%)	District Name	Building Density by Districts (%)
Şile	2	Çekmeköy	3
Bağcılar	31	Güngören	52
Kağıthane	24	Arnavutköy	6
Beşiktaş	17	Esenler	24
Fatih	39	Zeytinburnu	29
Kadıköy	30	Ümraniye	24
Küçükçekmece	15	Sultanbeyli	20
Adalar	3	Bahçelievler	38
Esenyurt	21	Sultangazi	12
Gaziosmanpaşa	45	Sarıyer	4
Bakırköy	13	Tuzla	8
Beylikdüzü	8	Ataşehir	22
Bayrampaşa	29	Başakşehir	6
Büyükçekmece	7	Beykoz	3
Eyüpsultan	5	Sancaktepe	10
Şişli	42	Avcılar	14
Üsküdar	22	Silivri	8
Kartal	20	Maltepe	14
Beyoğlu	40	Pendik	9
Çatalca	4		

2.2. Normalized Difference Vegetation Index (NDVI)

The NDVI index is a measure of the amount and vitality of surface vegetation. Considering that green vegetation containing chlorophyll reflects well in the near-infrared (NIR) part of the spectrum and absorbs well in the red (R) wavelength range in the visible region, the NDVI is calculated using Equation 2 [18].

$$NDVI = \frac{(NIR - R)}{(NIR + R)} \quad (2)$$

The NDVI result obtained is presented in Figure 1c. In this figure, NDVI values vary between -1 and +1, and values close to +1 represent areas with active vegetation and low (near-zero or negative) values indicate other types of materials [19]. To determine only the green areas from the NDVI image, the natural breaks Jenks algorithm was applied to the NDVI results. The resulted binary images indicating 0 (other areas) and 1 (vegetated areas) were given in Figure 1d.

2.3. Land Surface Temperature (LST)

The thermal band (Band 10) of the TIRS sensors of the Landsat 8 satellite was used to obtain the LST values. For the LST analysis, firstly, the numerical values (DN) were converted into spectral reflectance values using Equation 3 (4).

$$L_{\lambda} = \frac{(LMAX_{\lambda} - LMIN_{\lambda})}{(QCALMAX_{\lambda} - QCALMIN_{\lambda})} \times (DN - QCalmin) + LMin_{\lambda} \quad (3)$$

In this formula; L_{λ} shows the spectral radiance value, DN shows the numerical cell values, Lmin and Lmax show the minimum and maximum spectral reflectance values in the thermal band, QCalMin, and QCalMax show the calibrated minimum and maximum cell values [20]. Equation 4 was used to convert the obtained spectral reflectance values to temperature values.

$$T = \frac{K_2}{\ln\left(\frac{K_1}{L_{\lambda}}\right) + 1} \quad (4)$$

where, T represents the temperature value in Kelvin, and K1 and K2 are the calibration constants of the TIR band. In this case, K1 and K2 constants for the Landsat 8 TIR band 10 are 774.89 and 480.89, respectively.

The obtained land surface temperature distribution is shown in Figure 2. In this figure, the temperature distributions in the study area vary between 12.77 °C and 46.67 °C. Areas with high temperatures generally correspond to areas with dense urban objects, while areas with low land surface temperature generally correspond to wetlands and green areas obtained as a result of NDVI.

Considering the averages of LST values on a district basis (Table 3), it was determined that the lowest average temperature value was 22 °C in the Adalar district and the highest average temperature value was 33 °C in Gaziosmanpaşa district.

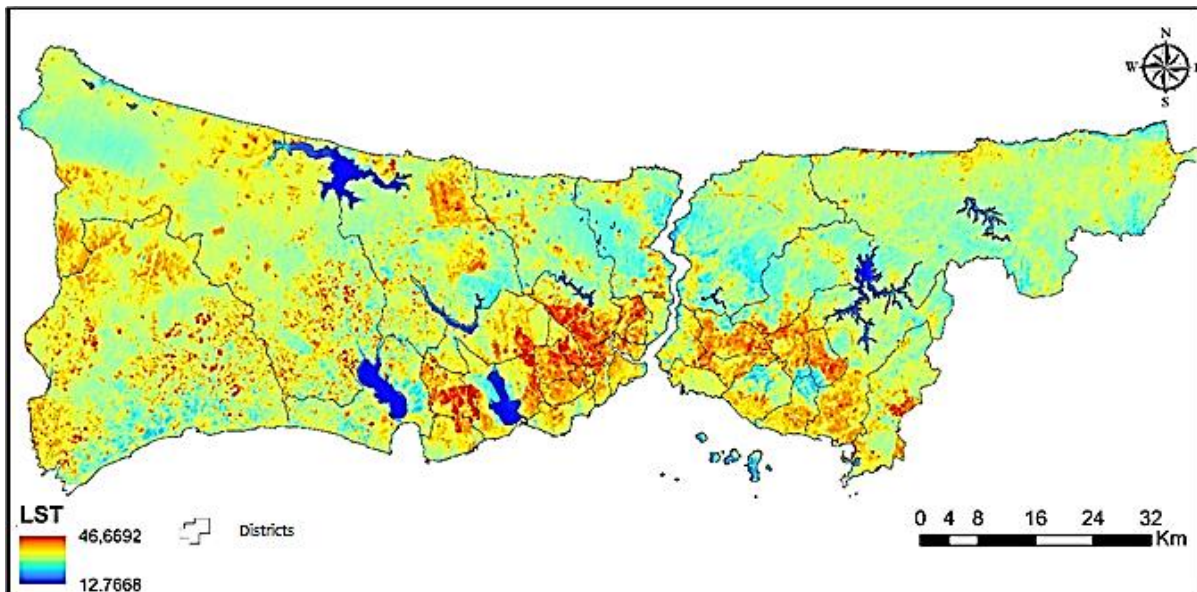


Figure 2. Land Surface Temperature Map (LST)

Table 3. Descriptive statistics of Land Surface Temperature (LST) by districts

District Name	Min (°C)	Max (°C)	Mean (°C)	District Name	Min (°C)	Max (°C)	Mean (°C)
Şile	16	37	26	Çekmeköy	17	36	26
Bağcılar	25	39	31	Güngören	27	35	31
Kağıthane	24	36	31	Arnavutköy	15	47	27
Beşiktaş	16	33	27	Esenler	24	36	30
Fatih	16	35	29	Zeytinburnu	18	36	29
Kadıköy	15	38	28	Ümraniye	22	43	30
Küçükçekmece	17	39	29	Sultanbeyli	21	36	30
Adalar	16	30	22	Bahçelievler	24	38	30
Esenyurt	23	44	31	Sultangazi	19	37	29
Gaziosmanpaşa	26	37	33	Sarıyer	14	37	26
Bakırköy	17	42	28	Tuzla	17	41	28
Beylikdüzü	17	41	28	Ataşehir	22	44	30
Bayrampaşa	25	46	32	Başakşehir	21	41	28
Büyükçekmece	17	42	27	Beykoz	14	36	26
Eyüpsultan	18	38	27	Sancaktepe	19	35	28
Şişli	24	35	30	Avcılar	18	37	28
Üsküdar	17	34	28	Silivri	17	45	28
Kartal	18	38	28	Maltepe	20	36	27
Beyoğlu	14	35	30	Pendik	17	40	27
Çatalca	16	38	27				

2.4. Evaluation of the relationship between land surface temperature and urban object ratio with pearson linear correlation

Correlation is a measure of the relationship between two variables. A change in the size of one variable in related data is related to the size of another variable in the same or opposite direction. This relationship value can vary between -1 and +1. Values close to -1 mean that the relationship is negative, and values close to +1 mean that the relationship is strong and positive [21].

The relationship between the two variables is determined by the Pearson Linear Correlation coefficient [22]. This correlation coefficient was developed by Karl Pearson (1857–1936). The Linear Correlation coefficient is given in Equation 5 [23].

$$r = \frac{n(\sum xy) - (\sum x)(\sum y)}{\sqrt{[n\sum x^2 - (\sum x)^2][n\sum y^2 - (\sum y)^2]}} \quad (5)$$

Where r is the Pearson Coefficient, $\sum xy$ is the sum of the product of the paired data, $\sum x$ and $\sum y$ are the sums of data, $\sum x^2$ and $\sum y^2$ are the sums of the squares of the data.

In this study, the averages of the land surface temperatures obtained in the districts and the percentage distributions of the urban object ratios in the districts were evaluated with the Pearson linear correlation method. According to the results obtained, the r value is 0.76. This value indicates that there is a positive relationship between these two variables.

3. Results and Discussions

As a result of the study, the building densities falling within each district boundary and the temperature values within the district boundaries were compared. According to the districts, the average surface temperature is the lowest at 22 °C, and the highest temperature is 33 °C. The district with the lowest temperature is Adalar, and the district with the highest temperature is Gaziosmanpaşa. When we look at the urban object ratios of the districts, the highest urban object ratio is Güngören district with 52%. The district with the lowest rate of urban objects is Şile with 2%.

The positive linear relationship between urban object ratios and surface temperatures is 76%. When the NDVI results are compared with the LST distributions, it is observed that the LST distributions show high values not only in urban areas but also in bare lands [24]. Urban areas, pavements, asphalt, buildings, etc., absorb and retain heat. surfaces are exposed to higher temperatures due to one reason for having high-temperature values for bare land is that most bare areas are devoid of vegetation. This leads to an increase in the amount of thermal energy emitted by the bare ground and hence an increase in temperature [24]. Green areas in urban areas have a positive effect on land surface temperature in terms of reducing the effect of urban heat island formation. Especially in these areas, the cooling effect through shadow and evaporation helps to regulate the urban climate and reduce the effect of the urban heat island [13,25]. In the study, urban and vegetated areas were extracted from 30 m resolution

bands. On the other hand, LST was extracted from a 100 m resolution thermal band. Therefore, the comparison was made with air temperature, which is different and can sometimes result in big differences [26]. Rapid changes in environment may adversely affect ecosystem [27]. As a result, the increase in vegetation and wetlands caused a decrease in LST values, while the building density in urban areas caused an increase in LST values and vice versa [14]. In the study, this situation was also confirmed by Pearson Linear Correlation.

4. Conclusion

This study described the relationship between land surface temperature and urban area, in Istanbul which is a densely urbanized city of Turkey. In the study urbanization density and LST are taken into account at the district base and the building densities falling within each district boundary and the temperature values within the district boundaries were compared. According to the districts, the average surface temperature is the lowest at 22 °C, and the highest temperature is 33 °C. The district with the lowest temperature is Adalar, and the district with the highest temperature is Gaziosmanpaşa. When we look at the urban object ratios of the districts, the highest urban object ratio is Güngören district with 52%. The district with the lowest rate of urban objects is Şile with 2%.

The comparison reveals that, the positive linear relationship between urban object ratios and surface temperatures, which amount is 76%. On the other hand, the spatial comparison of vegetation areas and urban areas with the LST distributions revealed that the LST distributions show higher temperature values in both urban and bare land.

Funding

This research received no external funding.

Author contributions

Gülcan Sarp: Data curation, Writing-Original draft preparation, Software, Validation, Writing-Reviewing, and Editing. **Emre Baydoğan:** Methodology, Software, Data Analysis, Visualization. **Firdevs Güzel:** Data Preparation, Literature Survey. **Tuğba Otlukaya** Formatting, and Literature Survey.

Conflicts of interest

The authors declare no conflicts of interest.

References

1. Kawamura, M., Jayamana, S., Tsujiko, Y. (1996). Relation between social and environmental conditions in Colombo Sri Lanka and the urban index estimated by satellite remote sensing data. *Int. Arch. Photogramm. Remote Sens.*, 31 (Part B7), 321–326.
2. Rikimaru, A., Miyatake, S. (1997). Development of Forest Canopy Density Mapping and Monitoring Model using Indices of Vegetation, Bare soil and Shadow. In *Proceeding of the 18th Asian Conference on Remote Sensing (ACRS) 1997*, Kuala Lumpur, Malaysia, 20–25 October 1997; p. 3.
3. Zhao, H.M., Chen, X.L. (2005). Use of Normalized Difference Bareness Index in Quickly Mapping Bare Areas from TM/ETM+. In *Proceedings of 2005 IEEE International Geoscience and Remote Sensing Symposium*, Seoul, Korea, 25–29 July 2005; 3, 1666–1668.
4. Xu, H. (2008). A new index for delineating built-up land features in satellite imagery. *Int. J. Remote Sens.* 29, 4269–4276.
5. Assayakur, R., Adnyana, S., Arthana, W., Nuarsa, W. (2012). Enhanced Built-Up and Bareness Index (EBBI) for Mapping Built-Up and Bare Land in an Urban Area. *Remote Sensing*, 2957-2970.
6. Meng, X., Cheng J., Zhao, S., Liu S., Yao, Y. (2019). Estimating Land Surface Temperature from Landsat-8 Data using the NOAA JPSS Enterprise Algorithm. *Remote Sensing*, 11, 155.
7. USGS (2021). <https://www.usgs.gov/core-sciencesystems/nli/landsat/using-usgs-landsat-level-1-data-product>.
8. Taha, H. (2004). Heat Islands and Energy. *Encyclopedia of Energy*, 133-143.
9. Jiang, J., Tian, G. (2010). Analysis of the impact of Land use/Land cover change on Land Surface Temperature with Remote Sensing. *Procedia Environmental Sciences* 2, 571-575.

10. Bokaie M., Zarkesh M., Arasteh P., Hosseini A. (2016). Assessment of Urban Heat Island Based on the Relationship between Land Surface Temperature and Land Use/Land Cover in Tehran. *Sustainable Cities and Society*, 94-104.
11. Sarp, G. (2016). Evaluation of Land Surface Temperature and Vegetation Relation Based on Landsat TM5 Data. *SCIREA Journal of Geosciences*, 1, 1-11.
12. Erener, A. & Sarp, G. (2017). Barajların Çevresel Etkilerinin Zamansal Ve Mekansal Olarak Uzaktan Algılama İle Değerlendirilmesi: Atatürk Barajı Örneği. *Geomatik*, 2 (1), 1-10. DOI: 10.29128/geomatik.300012
13. Sarp, G., Temurcin, K., Aldirmaz, Y. (2018). Evaluation of Industrialization Effects on Urbanization and Heat Island Formation Using Remote Sensing Technologies: A Case of Istanbul Bağcılar District. *Sdü Fen-Edebiyat Fakültesi Sosyal Bilimler Dergisi*, 6.
14. Zhang, F., Kung, H., Johnson, V. C., LaGrone B. I., and Wang J. (2018). Change detection of land surface temperature (LST) and some related parameters using Landsat image: a case study of the Ebinur lake watershed, Xinjiang, China. *Wetlands*, 38 (1), 65–80.
15. Temurçin, K., Sarp, G., Aldirmaz, Y., Kılıç, M. (2019). Şehirleşme İle Kentsel Isı Adası Oluşumu Arasındaki İlişkinin Jeoinformasyon Teknikleri İle Değerlendirilmesi: İstanbul Örneği. *Bilge Kağan 2 nd International Science Congress, Bilge Kağan ISC – 2019, 05-06-07 November 2019 Barcelona SPAIN*.
16. <https://earthexplorer.usgs.gov/>
17. Zha, Y., Gao, J., Ni, S. (2003.) Use of normalized difference built-up index in automatically mapping urban areas from TM imagery. *International Journal of Remote Sensing*, 583-594.
18. USGS (2022). <https://www.usgs.gov/landsat-missions/landsat-normalized-difference-vegetation-index>
19. Sarp, G. (2012). Determination of Vegetation Change Using Thematic Mapper Imagery in Afşin-Elbistan Lignite Basin; SE Turkey. *Procedia Technology*, 1, 407 – 411.
20. Chander, G., and Markham, B. (2003). Revised Landsat-5 TM Radiometric Calibration Procedures and Post Calibration Dynamic Ranges. *IEEE Transactions on Geoscience and Remote Sensing*. 41 (11), 2674-2677.
21. Schober, P., Boer, C., Schwarte, L.A. (2018). Correlation Coefficients: Appropriate Use and Interpretation. *Anesth Analg*. 126 (5), 1763-1768. <https://doi.org/10.1213/ANE.0000000000002864>. PMID: 29481436.
22. Pearson Correlation Coefficient (2021). <https://study.com/academy/lesson/pearson-correlation-coefficient-formula-example-significance.html> (Last access 23.02.2022)
23. STAT 462; Applied Regression Analysis <https://online.stat.psu.edu/stat462/node/96/> (Last access 23.02.2022)
24. Fonseka, H., Zhang, H., Sun, Y., Su, H., Lin., H. L. (2019). Urbanization and Its Impacts on Land Surface Temperature in Colombo Metropolitan Area, Sri Lanka, from 1988 to 2016. *Remote sensing*, 11(8), 957-975.
25. Gherraz, H., Guechi, I., & Alkama, D. (2020). Quantifying the effects of spatial patterns of green spaces on urban climate and urban heat island in a semi-arid climate." *Bulletin de la Société Royale des Sciences de Liège*, 89, 164-185.
26. Avdan U., Jovanovska G. (2016). Algorithm for Automated Mapping of Land Surface Temperature Using LANDSAT 8 Satellite Data. *Journal of Sensors*, 2016, 1480307. <https://doi.org/10.1155/2016/1480307>
27. Erener, A., & Yakar, M. (2012). Monitoring coastline change using remote sensing and GIS technologies. *Lecture Notes in Information Technology*, 30, 310-314.



© Author(s) 2021. This work is distributed under <https://creativecommons.org/licenses/by-sa/4.0/>







Advanced Remote Sensing

<http://publish.mersin.edu.tr/index.php/arcej>

e-ISSN 2979-9104



LST change for 16-year period for different land use classes

Burak Kotan¹, Abdullah Tatmaz¹, Suat Kılıç¹, Arzu Erener*¹

¹Kocaeli University, Department of Geomatics Engineering, Türkiye, bkotan19@gmail.com, atmaz7@gmail.com, suat64565@gmail.com, arzu.erenner@gmail.com

Cite this study: Kotan, B., Tatmaz, A., Kılıç, S. & Erener, A. (2022). LST change for 16-year period for different land use classes. *Advanced Remote Sensing*, 1(1), 38-45

Keywords

LST
Land use
Landsat
GIS

Research Article

Received: 17.11.2021
Revised: 13.12.2021
Accepted: 20.12.2021
Published: 30.12.2021

Abstract

Problems such as global warming and climate change have been increasing their impact in the world negatively in recent years. With the development of the industry, more factories were established. Thus, more harmful gases were released into the environment with more factories. This ultimately caused environmental pollution and eventually damage to the atmosphere. In pursuit of this, the rays coming to the Earth too much have triggered Global Warming. The earth's surface temperature is severely affected by the energy exchange between the earth and the atmosphere. The surface temperature can be measured by terrestrial measurements, but there are constraints in terms of continuity, time, and cost. In this sense, remote sensing is a technology that is fast, reliable, and provides an advantage over terrestrial measurements in terms of cost. Within the scope of this study, the 16-year process between the land surface temperature maps of Kocaeli Province was examined by remote sensing. In this context, Landsat 8 OLI_TIRS and Landsat 5 TM satellite images were used dated 02.07.2017 and 02.07.2001 respectively. Temperature changes were obtained for the different land uses and evaluated for 16-year period in the GIS environment.

1. Introduction

The data obtained by Meteorology Affairs from the point ground stations is one of the most used data in evaluating the ground surface temperature measurements. There are kilometers of distance between these stations, and the measured value can usually only represent that point and its surroundings. For this reason, obtaining information about each point on the surface is done by interpolation methods, this remains far from representing the real data. Because the earth is not just plains. It consists of high mountains, indented shapes, and mountainous areas. Variation in altitude and changes in land use will also bring about differences in surface temperatures. In this sense, stations representing the data of the surface pointwise are limited in producing continuous data. Images taken from satellites are used for land use map creation, classification, etc. although, they can be used in measuring the ground surface temperature. These images consist of bands. Each band has a reflectance value. The thermal infrared regions are providing data to create temperature distribution of surface. In the last 40 years, many studies have been carried out on the urban heat island to determine the ground surface temperature. In the literature, studies using satellite images and algorithms used for ground surface temperatures show diversity in the scientific field. Dağlıyar et al. [1] conducted a study in 2015 and determine the ground surface temperature of Kahramanmaraş province and its surroundings, using the data they received from the Landsat image. In the study carried out by [2], the relationship between urban heat island density and population in 10 different regions with populations ranging from 1000 to 2 million was investigated and compared their results with previous studies. Ndossi et al. [3] used Aster satellite images in their study. They compared three algorithms

for LST. In the study conducted by [4], the spatial effects of urbanization on heat island formation were examined with Remote Sensing Technologies. Landsat-8 OLI-TIRS and Sentinel-2 satellite images were used in the study. In the research, vegetation areas were obtained from Sentinel-2 satellite images, and urban area information was obtained using the normalized building difference index (NDBI). In the study by [5], time-series Landsat (TM and ETM+) satellite data products have been employed to quantify the spatiotemporal LST and Urban Heat Island (UHI) intensity for the years 2000, 2005, 2010, and 2015, respectively. Jain et al. [6] investigated the effect of changing LULC, at a local scale, on various variables-land surface temperature (LST), normalized difference vegetation index (NDVI), emissivity, albedo, evaporation, Bowen ratio, and planetary boundary layer (PBL) height, from 1991–2016. Rosas et al. [7] used 28 Landsat 8 satellite images between April and December 2015 in their study. Şekertekin and Marangoz [8] examine the impact of Land Use Land Cover (LULC) on Land Surface Temperature using Landsat 8 satellite data for Zonguldak metropolitan region. Orhan [9] investigated the effect of urbanization on the surface temperature of the city of Mersin. In this context, the Land Surface Temperature maps of the years 1990-1999-2007-2011-2018 were produced and, CORINE land use/cover data were used to identify urban areas in 1990 and 2018. Land surface temperature is an important parameter that shows or manages the energy balance on the earth and is an important factor that directs the dynamic change of environment and earth resources [10-11].

Different methods could be used for geospatial informations from relevant digital data in many disciplines [12-13]. GIS is a beneficial tool in evaluating the results obtained from satellite images [14]. Remote sensing and GIS technology is one of the essential tools in capturing spatial-temporal data and used for many applications intensively [14-15]. GIS is a tool for mapping and analyzing features and events on earth. Also, temperature changes can be obtained for the different land uses and evaluated in the GIS environment

Various algorithms exist for the determination of earth temperatures. The most widely used algorithm includes Land Surface Temperature – LST. Within the scope of this study, LST maps were created for different periods of different land use within the borders of Kocaeli province by using Landsat-5/8 satellite images. The Landsat data used were to a common day of each year. To reach the near or similar days of satellite images of different years, archive data was searched. The changes in the forest, agriculture, industry-urban, and seawater areas were examined from LST maps produced between 2001-2017.

2. Study Area and Data

The study region has been determined as the provincial border of Kocaeli, whose population and urbanization are increasing day by day due to 14 organized industrial zones and existing job opportunities (Figure 1). Kocaeli is located in the northwest of Turkey between 40.7655° latitude and 29.9407° longitude. In Kocaeli, which has a population of 1,883,270 million people for 2018, there are 521 people per square meter. The climate of the city, due to its special location, is a transitional climate between the Mediterranean climate and the Black Sea climate.

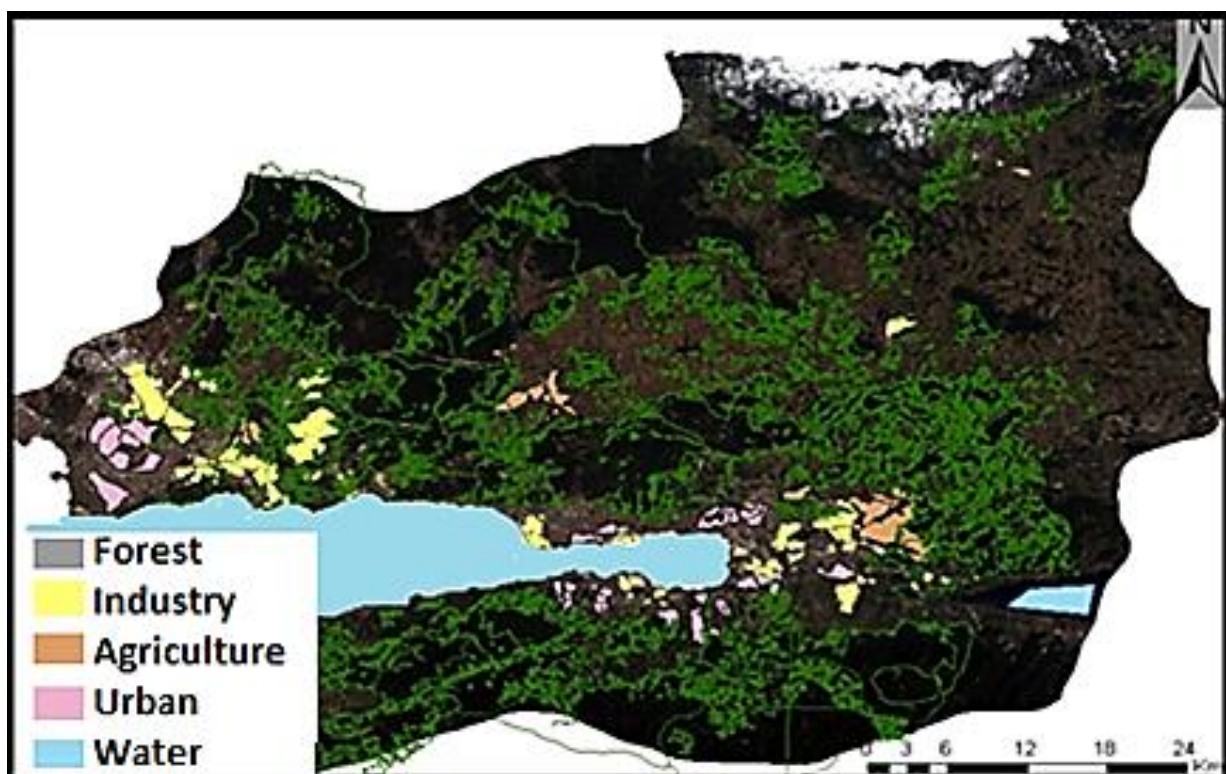


Figure 1. Kocaeli map and land use of the study area

The data used in this study are presented in Table 1. Landsat 5 and Landsat 8 satellite images taken in very recent months were used to determine the land surface temperature. These images were obtained from free satellite images available on the USGS website [16] and [17]. Meteorological data for Kocaeli province for the year 2001-2017 for the day the satellite image was taken were obtained from [18].

Table 1. Data used in the study

Data	Type	Data Used	Band	Spatial Resolution	Date
Meteorological Data	Point Data	Surface Temperature	-	-	2001-2017
Land Use Data	Polygon	Land use	-	-	2013
Remote Sensing Image	Landsat 5 TM	B6 Thermal	10.4-12.50	120x(30)	02.07.2001
	Landsat OLI_TIRS	B10 Thermal	10.60-11.19	100x(30)	02.07.2017

The Landsat-8 satellite image consists of a total of 11 spectral bands and has 2 separate thermal bands ranges from 10.6-11.19 μm , 11.50-12.51 μm . The spatial resolution of the visible and infrared range is 30 m. Bands 10 and 11 form the thermal bands of the satellite and its spatial resolution is 100 m. The satellite has a temporal resolution of 16 days. Landsat-8 satellite offers its products to its users with 16-bit radiometric resolution (Figure 2a). The Landsat-TM satellite image consists of a total of 7 spectral bands and the 6th band, which is in the range of 10.40-12 μm , constitutes the only thermal band of the satellite. The spatial resolution of the bands in the visible and infrared region is 30 m, and the spatial resolution of the 6th band in the thermal range is 120 m. Landsat-5 satellite, which has a temporal resolution of 16 days, offers its user's images with 8-bit radiometric resolution (Figure 2b).

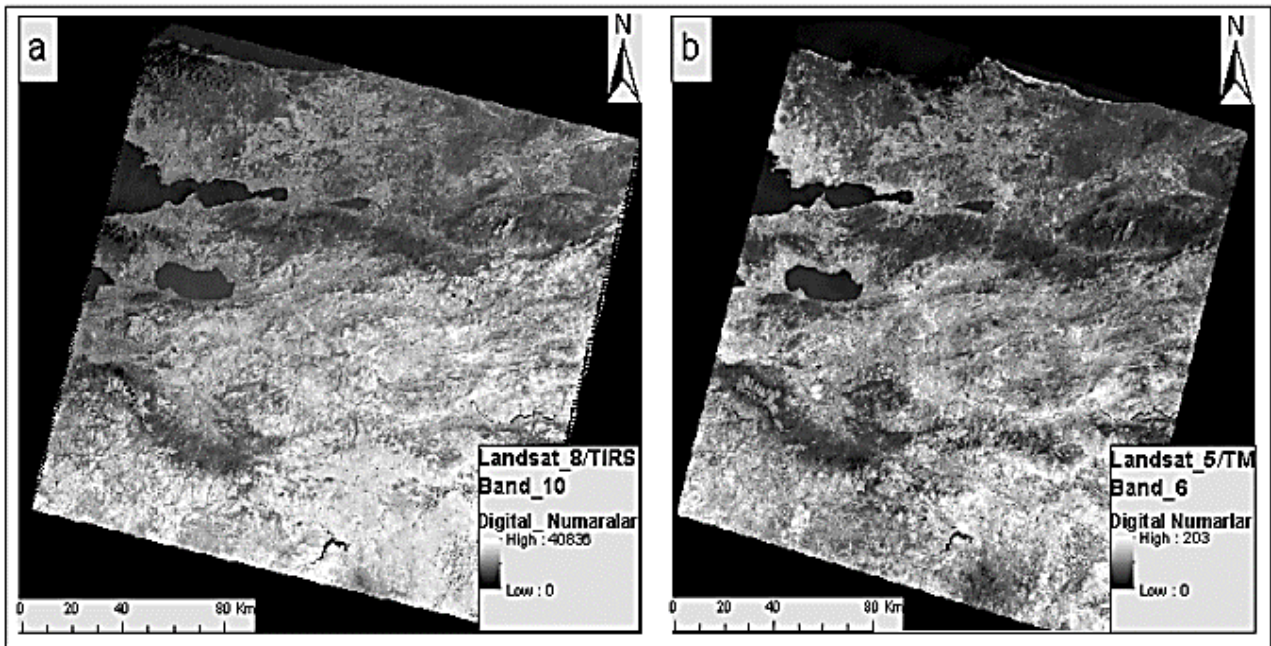


Figure 2. Raw data used in the study of Landsat satellite, a. Landsat8 (10th band), b. Landsat5 (6th band)

3. Land Surface Temperature (LST) Algorithm

In this study, a continuous surface temperature map of Kocaeli was calculated using the Land Surface Temperature algorithm. Since the radiance values are used while calculating the surface temperatures, the numerical values of the satellite data should be converted to the radiance value. The effect of land cover and topography should be taken into account when interpreting the radiant temperature image [19].

For this purpose, initially by using Equation (1), the pixel values of the thermal band were converted into spectral radiance (L_λ) values. Radiance is the amount of energy reflected from the field at a certain wavelength at a certain angle [1,20-21].

$$L_\lambda = L_{\min} + \left(\frac{L_{\max} - L_{\min}}{Q_{\max}} \right) Q_{cal} \quad (1)$$

L_λ - spectral radiances, Q_{cal} digital numbers of the relevant band, $L_{max-min}$ values were obtained from the metadata file of the data.

The radiance value consists of the thermal dissipation component, which is formed due to the temperature of the material on the earth's surface being above zero, the radiation when the atmosphere temperature is above absolute zero, the absorption and refraction of the radiation made by the material in the atmosphere and the components that occur as a result of atmospheric events. To correct these, the radiance values for the thermal band (10th band) of the Landsat 8 TM satellite data and the thermal band (6th band) of the Landsat 5 TM satellite data should be converted to luminance temperature values [19].

$$T_R = \frac{K_2}{\ln\left(\frac{K_1}{L_\lambda} + 1\right)} \quad (2)$$

T_R luminance temperature value on the sensor (K), K_1 is the first calibration constant, K_2 is the second calibration constant, L_λ is the spectral radiance at the sensor.

Table 2. Calibration Constant

Satellite	K_1	K_2
Landsat 5 TM	607.76	1260.56
Landsat 8 OLI_TIRS	774.8853	1321.0789

Surface temperature; L_λ radiance, T_R : luminance temperature value on the sensor, and the ϵ surface emissivity value is calculated together [22].

$$LST = \frac{TB}{1 + \left(\lambda * \frac{T}{h * c / s}\right) * \ln(\epsilon)} \quad (3)$$

Here, LST is the surface temperature (K), T_B is the blackbody temperature (K), λ is the wavelength of the reflected radiance (μm), $\alpha = hc/s$ ($1.438 \times 10^{-2} M_k$).

Surface temperature maps were created by applying Equations 1, 2, and 3 to the downloaded satellite images for the study area, respectively, in the information technology environment.

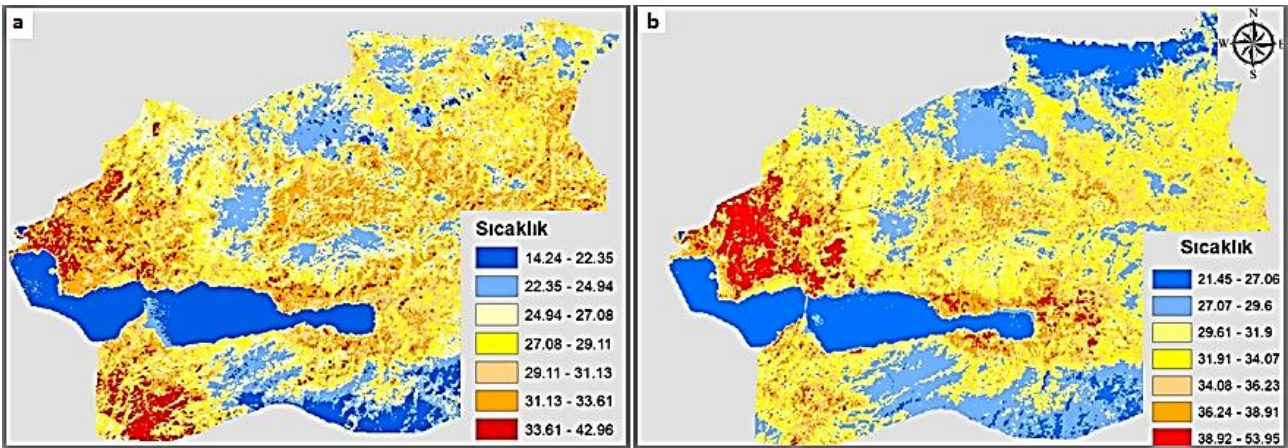


Figure 3. Landsat surface temperature maps, **a.** 02.07.2001 Landsat 5 TM, **b.** 02.07.2017 Landsat 8 OLI_TIRS

The surface temperature map of Kocaeli province is presented in Fig. 3 for 2001 and 2017. It is evident from the observation that the temperature is very high within the city core as well as certain surrounding areas of the city, especially on the northern side. The temperature is comparatively lower on the eastern side of the city than in the western region. Certain peripheral regions, however, show a higher temperature. This can be due to the development taking place in the outer areas of the city and the destruction of vegetation in the outlying parts of the city. In particular, the increase in industry and urban construction can be considered as the cause of the increase in LST. The results were also compared with the meteorological temperature values. The LST values obtained from the satellite image are obtained continuously for the whole area, and it is not very meaningful to compare the continuous data with the data obtained from the point-based meteorological station. However, for

the general evaluation, the temperature averages obtained for the LST and meteorological data were compared. Accordingly, the surface temperature values obtained from the satellite and the meteorological temperature values have a temperature difference of 5-6 degrees from each other. The satellite data and the meteorological temperature in 2001 and 2017 increased 5.16 °C and 5.07 °C respectively. Since the temperature values obtained from the satellite image are obtained continuously and within the scope of the entire area, it is considered normal to see this temperature difference between the data obtained pointwise from the meteorological station and not exactly overlap. In addition, the fact that the surface temperature data obtained from satellite images cover the entire region also offers an advantage in terms of detecting the differences between different land-use areas.

4. Discussion

The temperatures in the LST maps obtained from the study were compared temporally for different land use areas. In this context, changes in temperatures in different land uses were observed. For this reason, temperature images and land use maps were overlapped. Sufficient samples were taken from the temperature images for the forest, agriculture, industry and urban, and seawater. The temperature values at the sampling points for the years 2001 and 2017 were assigned to the databases of these random points. For these values, a new column was created on the database and the difference values were obtained by taking the difference of the 2001-2017 temperature values from each other. For each land-use area, the temperature distributions of the same point in different years were created.

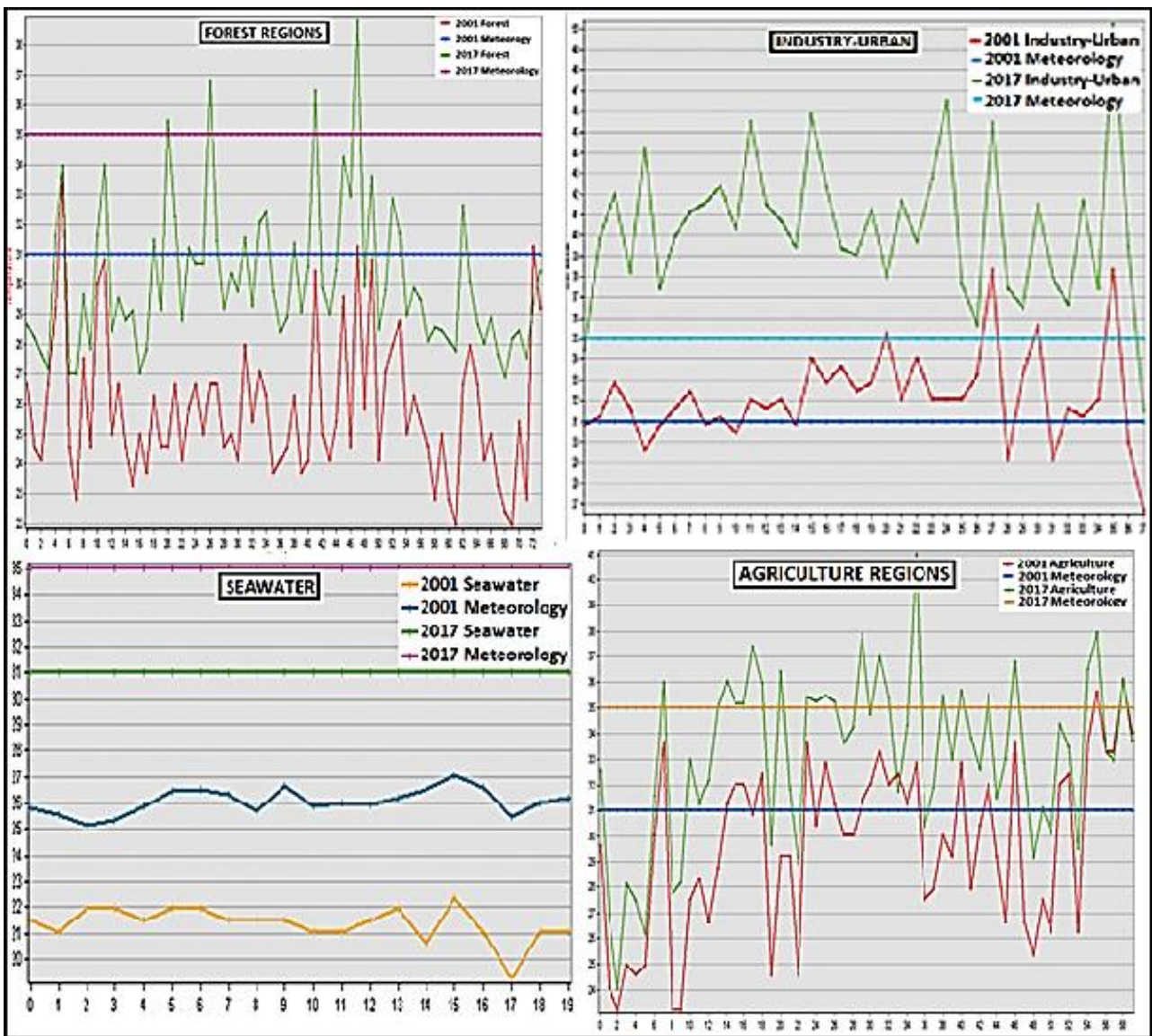


Figure 4. Temperature changes in different land use classes

It was observed that the 2017 and 2001 temperature values for the forest area range between 27 °C to 39 °C and 22 °C to 31°C, respectively. The meteorological temperature for 2017 and 2001 was on average 35°C and 31°C. It was clear that both of the values were increased in 2017 compared to 2001 for forest regions. Similarly, an increase in temperature was observed in other land uses in 2017 compared to 2001. For the agricultural area, 5 °C differences were observed for the maximum temperature values between 2017 and 2001. On the other hand, the temperature difference is quite high for industrial and urban regions. 2017 and 2001 temperature values for the industrial and urban regions range between 50 °C to 31 °C and 39 °C to 27 °C, respectively. As can be seen in the temperature graph for the industrial-urban area, it was observed that the temperature values were higher for 2017 compared to 2001. As can be seen from the temperature graph for the seawater area, it was observed that the temperature values in the sea area were higher for 2017 compared to 2001.

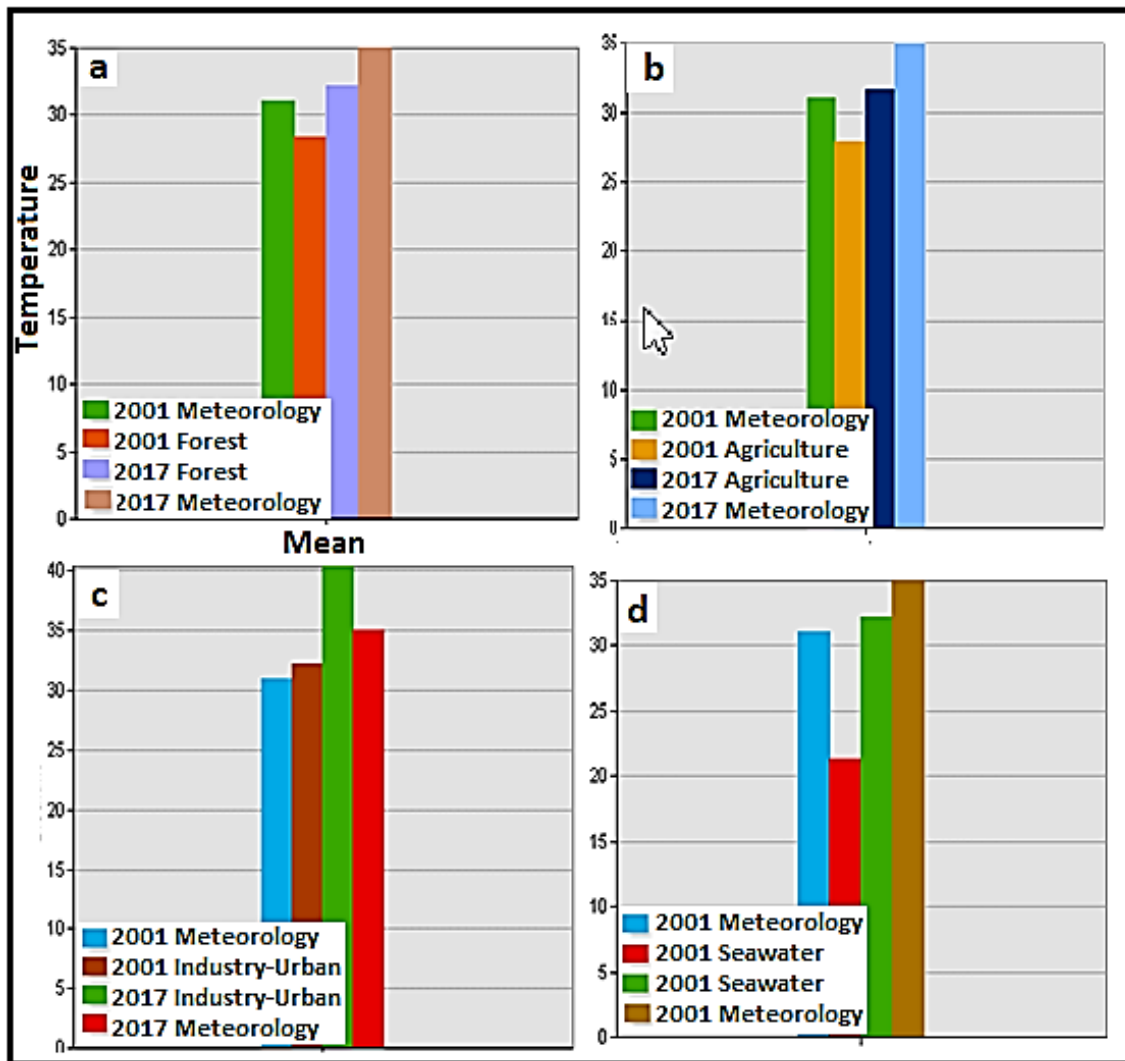


Figure 5. Average temperature changes between 2017 to 2001 for meteorology and different land uses **a.** Forest, **b.** Agriculture, **c.** Industry-Urban, **d.** Seawater

The average temperatures were calculated for the temperature variation differences in the land use areas. While the average was 28 °C in 2001, it was determined to be around 32 °C in 2017 for forest regions. In agricultural areas, the average difference between meteorological stations increased by 5 degrees from 2017 to 2001, while this increase is about 4 degrees according to the points above LST. On the other hand, while the average difference over LST between 2017 and 2001 for industry-urban regions increased by 9 °C, this difference increased by 4 °C in meteorological stations. A similar situation is observed in seawater areas. While the difference in temperature averages over LST in 2017-2001 increased by 10 °C, the increase between the meteorological station averages was 4 °C approximately.

5. Conclusion

Increasing urbanization and industrialization have caused the air temperature to rise due to the pollution of the environment and atmosphere. This change has occurred as an environmental factor that negatively affects the life of living beings. Therefore, remote sensing technology and surface temperature research have made progress in this direction. In the study, the land surface temperature of Kocaeli Province was determined with the help of remote sensing techniques from the Landsat 5 TM image dated 2001/07/02 and the Landsat 8 OLI TIRS image dated 2017/07/02. When the LST maps were examined, it was observed that the temperature increased around the bay in the 16 years. As a result of the study, the comparison of surface temperatures according to 16-year period was made for four different land uses. Accordingly, it was observed that temperature increased from 2017 to 2001 in all land use areas. An average temperature of 4 °C, 5 °C, 9 °C, and 10 °C increased in the forest, agricultural, industrial-urban, and seawater areas in Kocaeli Province.

According to the results, the average temperatures have increased, especially in industrial-urban and seawater areas. This temperature increase may be meaningful with the increase in sea pollution and industrial factories with the increasing population. However, it should not be forgotten that the satellite image reflects the day it was taken and provides information about the weather conditions of that day. People who affect the observed temperature changes need to be more sensitive to the environment and nature and behave carefully. It is recommended not to harm biological activities by reducing all kinds of harmful effects such as vehicle density and exhaust, building density, uncontrolled factory fumes, chemical products, etc., which are harmful to the atmosphere and cause temporal temperature differences, which are defined as global warming. There has been a decrease in forest areas as a result of uncontrolled and rapid construction arising from the increase in migration to settlements. It is recommended that due care and diligence be shown to increase these green areas again.

Acknowledgement

This study was constructed as an undergraduate thesis study under the supervision of Arzu Erener in 2018.

Funding

This research received no external funding.

Author contributions

Burak Kotan: Investigation, Writing-Original draft preparation, Writing-Reviewing, and Editing. **Suat Kılıç and Abdullah Tatmaz:** Visualization, Investigation, Data curation, Software, Validation. **Arzu Erener:** Conceptualization, Methodology, Investigation, Writing-Original draft preparation, Writing-Reviewing

Conflicts of interest

The authors declare no conflicts of interest.

References

1. Dağlıyar, A., Avdan, U., Uça Avcı Z. D. (2016). Uzaktan Algılama Verileri Yardımıyla Kahramanmaraş ili ve Çevresinin Yer Yüzey Sıcaklığının Belirlenmesi, TUFUAB VIII. Teknik Sempozyumu 21-23 Mayıs 2015 / Konya, 324-331
2. Oke T.R. (1973). City size and the urban heat island, Atmospheric Environment. 7(8), 769-779.
3. Ndossi, M.I. & Avdan U. (2016). Inversion of Land Surface Temperature (LST) Using Terra ASTER Data: A Comparison of Three Algorithms, Remote Sensing. 8(12).
4. Erener, A. & Sarp, G. (2017). Kentleşmenin Isı Adaları Oluşumu Üzerine Etkisinin Uzaktan Algılama Teknolojileri ile Değerlendirilmesi, I. Uluslararası Bilimsel ve Mesleki Çalışmalar Kongresi, Nevşehir, Türkiye
5. Jain, S., Sannigrahi, S., Sen, S., Bhatt, S., Chakraborti, S., Rahmat, S. (2020). Urban heat island intensity and its mitigation strategies in the fast-growing urban area, Journal of Urban Management. 9(1): 54-66
6. Jain M., Dimri A.P., Niyogi D. (2017). Land-Air Interactions over Urban-Rural Transects Using Satellite Observations: Analysis over Delhi, India from 1991–2016, Remote Sensing, 2017, 9(12).
7. Rosas, J. Houborg, R. & McCabe, M.F. (2017). Sensitivity of Landsat 8 Surface Temperature Estimates to Atmospheric Profile Data: A Study Using MODTRAN in Dryland Irrigated Systems, Remote Sens. 9(10), 988 <https://doi.org/10.3390/rs9100988>

8. Şekertekin, A. & Marangoz, A. M. (2019). Zonguldak Metropolitan Alanındaki Arazi Kullanımı Arazi Örtüsünün Yer Yüzey Sıcaklığına Etkisi. *Geomatik*, 4 (2), 101-111. DOI: 10.29128/geomatik.497051
9. Orhan, O. (2021). Mersin İlindeki Kentsel Büyümenin Yer Yüzey Sıcaklığı Üzerine Etkisinin Araştırılması. *Geomatik*, 6 (1), 69-76. DOI: 10.29128/geomatik.679858
10. Şekertekin, A. İ. (2013). Uzaktan algılama verileri ile bölgesel çevre etkilerinin belirlenmesi: Zonguldak Örneği, Bülent Ecevit Üniversitesi Fen Bilimleri Enstitüsü Jeodezi ve Fotogrametri Mühendisliği Ana Bilim Dalı, Yüksek Lisans Tezi, Zonguldak
11. Qin Z., Karnieli A., Berliner P., A (2001). Mono-Window algorithm for retrieving land surface temperature from Landsat TM data and its application to the Israel-Egypt Border Region, *International Journal of Remote Sensing*. 22(18), 3719-3746
12. Yılmaz, H. M., Yakar, M., Mutluoglu, O., & Yildiz, F. (2004, July). Selection of the most suitable sizes of ground control points in the satellite images. In *ISPRS Congress Istanbul*, 12-13.
13. Mutluoğlu, Ö., Yakar, M., & Yılmaz, H. M. (2016). Investigation of spatial accuracy of high-resolution (50cm) Worldview-2 satallite images. *Selçuk Üniversitesi Mühendislik, Bilim ve Teknoloji Dergisi*, 4(4), 321-329.
14. Erener, A., & Yakar, M. (2012). Monitoring coastline change using remote sensing and GIS technologies. *Lecture Notes in Information Technology*, 30, 310-314.
15. Mutluoglu, O., Yakar, M., & Yılmaz, H. M. (2015). Investigation of effect of the number of ground control points and distribution on adjustment at WorldView-2 Stereo images. *International Journal of Applied Mathematics, Electronics and Computers*, 3(1), 37-41.
16. <https://earthexplorer.usgs.gov/>
17. <http://libra.developmentseed.org/>
18. <https://www.meteoblue.com/tr>
19. Çapar, N. (2009). Landsat uydu görüntüleri kullanılarak jeotermal kaynakların araştırılması, Ankara Örneği Yüksek Lisans Tezi, İstanbul Teknik Üniversitesi, Fen Bilimleri Enstitüsü, Jeodezi ve Fotogrametri Mühendisliği Anabilim Dalı, Haziran 2009, İstanbul, Türkiye
20. Grupta, R. P. (2015). *Remote Sensing Geology*, Second Edition, Almanya, Springer – Verlag.
21. Yıldız, A., Bağcı, M., Başaran, C., Çonkar, F. E., Ayday, C. (2017). Landsat 8 Uydu Verilerinin Jeotermal Saha Araştırmalarında Kullanılması: Gazlıgöl (Afyonkarahisar) Çalışması, *Afyon Kocatepe Üniversitesi Fen ve Mühendislik Bilimleri Dergisi*, 17, 277-284.
22. Artis, D.A., Carnahan, W.H. (1982). Survey of emissivity variability in thermography of urban areas, *Remote Sensing of Environment*, 12(4), 313 – 329



© Author(s) 2021. This work is distributed under <https://creativecommons.org/licenses/by-sa/4.0/>